Diamond & Related Materials 171 (2027) 114313

Contents lists available at ScienceDirect

Diamond & Related Materials

journal homepage: www.elsevier.com/locate/diamond

Plasma etch process optimization for photonic-grade diamond-on-insulator substrates and thickness evaluation using colorimetry

Tianyin Chen [a,*,1], Alessio Miranda [a,b,1], Leyla Rami [a,b], Ryoichi Ishihara [a,b], Salahuddin Nur [a]

[a] Department of Quantum Computer Engineering, Faculty of Electrical Engineering, Mathematics and Computer Science, Delft University of Technology, Delft, The Netherlands

[b] QuTech, Delft University of Technology, Delft, The Netherlands

ARTICLE INFO

Keywords:
Plasma etch
Diamond on insulator
Debonding prevention
Surface-quality control
Free-standing diamond chiplet
Colorimetry

ABSTRACT

Diamond qubits integrated with photonic circuits can be initialized, manipulated, entangled, and read out individually with high fidelity, making them attractive for large-scale quantum systems. However, the limited size of heteroepitaxially grown single-crystal diamond and photonic-grade diamond-on-insulator (DOI) remains challenging for integration with existing manufacturing processes. Here, we develop a plasma etch recipe to thin direct-bonded (100) single-crystal diamond (< 50 μm) into large-area, thin-film DOI, and demonstrate free-standing photonic chiplets fabricated from the resulting DOI. The ICP-RIE recipe preserves bonding and provides sufficient micro-masking and surface-quality control. We thin a 10 μm diamond bonded to SiO_2/Si and obtain a photonic-grade DOI with diamond thickness ≤ 300 nm over 0.5×0.5 mm^2 with roughness < 0.5 nm. Diamond photonic chiplets are fabricated using a standard two-step lithography process, without complex thin-film transfer, under-etching, or pedestal formation. We also present a colorimetric study of diamond visibility and quantify color differences across thicknesses in common colorimetric spaces. This analysis enables automatic diamond-thickness extrapolation from standard optical microscope images with 5 nm resolution, in good agreement with white-light interferometry (WLI) measurements. The DOI substrate and colorimetric thickness-evaluation method provide an effective fabrication platform and reliable validation route for scalable manufacturing of diamond nanophotonic devices.

1. Introduction

Diamond has become one of the leading material platforms for quantum technologies [1–6] and extreme-environment devices. This broad relevance arises from its combination of an ultra-wide bandgap (≈ 5.47 eV), exceptional thermal conductivity (~2200 W m^{-1}·K^{-1}, among the highest of natural materials), high mechanical stiffness, optical transparency from the UV to the mid-IR, and chemical robustness [2,7–13]. In conventional device domains, these properties underpin low-loss photonics, including Raman lasers and nonlinear optics, optoelectronic components, and extreme-environment electronics with high breakdown fields and efficient heat dissipation [7–15]. Beyond its bulk material properties, diamond hosts atom-like point defects, or color centers, including the nitrogen-vacancy (NV) center and group-IV split-vacancy centers such as SiV, GeV, and SnV. These defects provide optically addressable electronic spins with long coherence and spin-selective optical transitions [5,6,16–19]. As a result, diamond color centers have become attractive building blocks for quantum computing, quantum communication networks, and distributed quantum sensing systems. They have already enabled diamond-based single-photon sources [3,16,20,21] quantum sensing systems [16,22–25], long-lived quantum memories [26–28], and landmark demonstrations including spin–photon entanglement and multi-node quantum networking [1,6,28–30].

Realizing practical systems based on these solid-state qubits requires efficient spin–photon interfaces and low-loss on-chip routing [16–18,31–34]. Embedding color centers in nanophotonic structures, such as waveguides, microdisks/rings, and photonic-crystal (PhC) cavities, enhances emission into useful optical modes, increases collection efficiency, and enables cavity-QED regimes in which Purcell enhancement

* Corresponding author.
E-mail addresses: T.Chen@tudelft.nl (T. Chen), alessio.miranda.tudelft@gmail.com (A. Miranda), rami.leyla.1@gmail.com (L. Rami), R.Ishihara@tudelft.nl (R. Ishihara), S.Nur@tudelft.nl (S. Nur).
[1] These authors contributed equally to this work.

https://doi.org/10.1016/j.diamond.2026.114313
Received 25 August 2026; Received in revised form 17 October 2026; Accepted 20 October 2026
Available online 2 November 2026
0925-9635/© 2026 The Authors. Published by Elsevier B.V. This is an open access article under the CC BY license (http://creativecommons.org/licenses/by/4.0/).

accelerates coherent photon generation and can improve entanglement rates [6,16–18,32,35–37]. Recent progress highlights this opportunity: thin-film diamond PhC cavities with record visible-wavelength quality factors of $Q \approx 1.6\text{–}1.8 \times 10^5$ have been demonstrated, and group-IV centers such as SnV^- have shown strong cavity-enhanced emission with large β-factors in nanostructures [6,16,18,35–40].

However, the transition from one-off diamond devices to scalable integrated circuits remains constrained by materials, substrate availability, and processing realities. High-quality, uniform thin single-crystal diamond (SCD) layers are still difficult to realize at scale. Commercial high-purity SCD is typically available only as small plates (mm–cm scale), while wafer-scale SCD by direct heteroepitaxy remains challenging due to nucleation, lattice and thermal-expansion mismatch, residual strain, mosaicity, and high dislocation densities [16,31,36,37,39–47]. Consequently, much of high-performance SCD nanophotonics has relied either on directly machining free-standing structures from bulk diamond, using angled/quasi-isotropic etching or focused-ion-beam methods, or on fabricating and transferring thin membranes derived from bulk through ion-slicing, overgrowth, or smart-cut-like approaches. These routes have enabled state-of-the-art proof-of-principle devices, including high-Q cavities, waveguides, and resonators. Nevertheless, they remain limited by throughput, design flexibility, surface damage, membrane area, variability in surface quality and thickness uniformity, and roughness on the back surface and pedestal formation. These parameters directly affect optical scattering loss, cavity yield, resonance reproducibility, spectral matching to color-center transitions, and ultimately the scalability of diamond quantum photonic circuits [16,31,37,41,42,48–51].

In conventional bulk-diamond free-standing fabrication routes, such as quasi-isotropic oxygen etching, the undercut is governed by crystal-plane-dependent etch profiles and by the local geometry of the patterned structure [41,52,53]. As a result, quasi-isotropic etching can naturally form pedestal-supported suspended devices, as reported for monolithic diamond microdisks, where an hourglass-shaped pedestal remains beneath the released disk [52]. For more complex layouts, such as cross-waveguide or intersecting-waveguide structures [54], this geometry-dependent undercut can make complete release more difficult, as different arms and junction regions may provide different etch-access paths and can leave residual support regions unless the release is carefully engineered. In contrast, the DOI process uses the buried SiO_2 as a sacrificial layer, enabling a more direct release, when necessary, of frame-supported diamond photonic chiplets for pick-and-place type heterogeneous integration.

In this work, we address the manufacturing bottlenecks by developing and validating a plasma-etch process for photonic-grade DOI starting from direct-bonded (100) SCD membranes (< 50 μm). We optimize an ICP-RIE recipe that alternates etching and surface-cleaning steps to (i) suppress debonding during aggressive thinning, (ii) minimize micromasking and nanopillar formation, and (iii) deliver smooth, uniform films suitable for nanophotonics. Using this process, we thin a 10 μm bonded diamond plate on SiO_2/Si down to ≈300 nm while maintaining sub-nanometer roughness over a 0.5×0.5 mm^2 area and preserving the bonding interface, meeting practical targets for integrated diamond waveguides and cavities.

Furthermore, to support rapid and accessible metrology during thinning, we develop a colorimetry-based thickness evaluation method tailored to diamond/SiO_2/Si stacks. By analyzing color distances across standard color spaces for different diamond/SiO_2 thickness combinations, we establish a robust mapping from optical micrographs to diamond film thickness with ≈5 nm resolution. This mapping is validated against white-light interferometry (WLI). The method provides a low-cost, microscope-based gauge for tracking the thinning process, shortening plasma-etch optimization cycles and enabling large-area uniformity checks without specialized thickness-metrology instrumentation.

Taken together, the optimized plasma thinning process, the frame-supported photonic chiplet demonstration and the colorimetric thickness evaluation provide a practical route to photonic-grade DOI substrates with the surface quality and thickness control required for reproducible diamond photonic device fabrication. Although the primary motivation is to advance diamond quantum nanophotonics towards scalable, heterogeneously integrated, and ultimately 3D-integrated systems, the same DOI platform and metrology are also relevant to classical diamond photonics, optoelectronics, and high-power or extreme-environment diamond electronics. The processing methodology, therefore, extends beyond quantum applications and provides a broadly applicable route for manufacturing thin, device-ready single-crystal DOI substrate.

2. Current status of thin-film diamonds

To realize large-scale integrated diamond photonic circuits, a suitable substrate architecture is required. A leading monolithic candidate is the diamond-on-insulator (DOI) platform, consisting of a thin, photonic-grade SCD membrane bonded to a low-refractive-index substrate, typically silicon dioxide (SiO_2) on a silicon handle wafer [16,37,47,51]. This architecture is analogous to the silicon-on-insulator (SOI) platform that transformed microelectronics and silicon photonics [56–58]. In DOI, the strong vertical refractive-index contrast between diamond ($n \approx 2.4$) and SiO_2 ($n_{SiO_2} \approx 1.45$) enables tight optical confinement in the diamond layer, supporting compact waveguides and high-Q cavities. This represents a shift from proof-of-principle experiments on individual color centers or released devices towards engineered, scalable, and integrated diamond quantum photonic systems. Analogous to SOI in silicon photonics [57,59–62], DOI can avoid complex diamond undercut steps [16,41,48,52,53,63–65] and enable planar processing of high-index-contrast waveguides, 1D/2D PhC cavities, couplers, and more complex photonic circuits. It also provides a natural route to dense integration with detectors, electrodes, and heterogeneous materials. Recent thin-film DOI-like platforms have already demonstrated high-Q cavities and uniform device arrays [16,37,51], provided that the diamond film offers: (i) a few-hundred-nanometer thickness suitable for single-mode guiding, (ii) low surface roughness, typically below ~1 nm over device areas, to suppress optical scattering, and (iii) low total-thickness variation (TTV) to maintain spectral uniformity across a chip.

Epitaxial growth of SCD on non-diamond substrates remains highly challenging. Although heteroepitaxial diamond has been demonstrated on specialized crystalline templates, most notably Ir-based buffer stacks, these approaches require complex lattice and thermal-expansion management and still suffer from mosaicity, residual strain, and dislocations. In contrast, direct growth or deposition of a photonic-grade SCD film on low-index oxide substrates such as SiO_2 has not been demonstrated, to the best of the present literature. Reported diamond growth on SiO_2 or fused silica typically yields microcrystalline, nanocrystalline, or polycrystalline diamond rather than photonic-grade SCD [16,41,45–47,53,66,67]. Therefore, bonding of pre-existing SCD plates remains so far the most practical route to attach diamond to low-index oxide materials and realize DOI substrates [16,37,41,42,47,51,53]. Among the available bonding approaches, hydrophilic direct bonding is particularly attractive because it enables direct bonding of (100) SCD plates to plasma-enhanced chemical vapor deposition (PECVD)-grown SiO_2/Si substrates at low temperature and atmospheric conditions, as demonstrated in our previous work [47]. However, producing large-area, photonic-grade DOI substrates with film thicknesses near or below 300 nm remains challenging to date [16,37,41,42,47,51,53].

Several groups have explored photonic-grade SCD membrane or film fabrication using processes similar to the smart-cut technology [16,41,43,49–51,68]. These approaches can produce high-quality membranes, but they typically require many demanding and expensive

Table 1
Brief comparison of representative thin-film diamond and diamond-on-insulator (DOI) approaches.

Category	High group, Chicago [51]	High/ Lončar [37]	Maletinsky group* [55]	IonQ platform* [40]	Our work
Technique	Direct-bonded released membranes	Bonded thin-film diamond cavity platform	Thinning-down etch; free-standing membranes	Thermocompression-bonded membrane transfer + thinning	Thinning-down etch on directly bonded DOI
Area / roughness	200×200 μm^2/NR	~ 200×200 μm^2/< 0.3 nm	mm-scale/< 0.2 nm	0.5 mm hexagonal membranes/< 0.3 nm	500×500 μm^2/< 0.5 nm
Thickness / variation	Down to 10 nm/nm-scale variation	160 nm/~1 nm variation	Down to 70 nm/< 0.35 nm/μm	160 nm/post-bond thin films demonstrated	~300 nm/< 0.08 nm/μm
Bonding / support	Directly bonded to Si, SiO_2, fused silica, sapphire, $LiNbO_3$	Bonded to SiO_2/Si; Cr/Au frame used	Free-standing membrane	Gold thermocompression bonding to semiconductor substrate	Plasma-activated hydrophilic bonding to SiO_2/Si
Key point	Multi-substrate heterogeneous bonding	High-Q visible cavities	Best recent free-standing uniformity	Scalable membrane transfer and integration	Simple bonded-on-Si DOI with in-line colorimetry
Relative position vs this work	True bonded stack, but much smaller area	Strong device result, but smaller area and added metal-frame complexity	Excellent area and uniformity, but not a true DOI stack	Scalable, but uses metal-interlayer thermocompression and a more complex transfer route	True DOI on SiO_2/Si; larger photonic-grade bonded area; no metal interlayer; preserved buried interface; simple, scalable process

DOI - diamond-on-insulator, NR - not reported. * Not a true DOI stack.

steps, including ion implantation to create a buried damage layer, SCD overgrowth, membrane lift-off, transfer printing, and complex membrane bonding. As a result, the produced membranes have so far remained limited in area (≤ 250 μm) and scalability for large photonic circuits and 3D-integrated on-chip quantum systems [16,37,50,51]. Only recently, a membrane area of 500 × 500 μm^2 has been reported using process steps such as ion implantation, membrane liftoff, high-quality overgrowth, and flip-chip bonding with metal pads [40]. However, this process produces free-standing membranes for photonic structures rather than a conventional DOI substrate, which limits its compatibility and scalability with all-diamond photonics and subsequent 3D-integration steps [40].

The central material-processing challenge is, therefore, to thin and planarize direct-bonded or transferred SCD membranes into photonic-grade DOI films while preserving both surface and interface quality. Dry etching is indispensable for this step [53], but oxygen-based inductively coupled plasma reactive ion etching (ICP-RIE) of diamond is sensitive to micromasking from particulates or redeposition, can generate nanopillars and pits, and may induce roughness that degrades optical performance [53,69–73]. Process windows that combine efficient material removal with smoothing or cleaning steps, such as cyclic O_2 and Ar/Cl_2 plasmas, can mitigate these effects and achieve sub-nanometer roughness suitable for high-finesse optics and cavity-QED [53,69–74]. In parallel with surface quality, bonding interfaces are critical for DOI reliability, thermal budgets, and 3D integration. Hydrophilic direct bonding of diamond to SiO_2/Si is attractive because it avoids metallic or polymeric interlayers that can introduce absorption, stress, or contamination detrimental to qubit coherence and photonic loss [16,47,51]. Recent work has demonstrated direct bonding of (100) diamond to deposited SiO_2 at low temperature, with interfacial chemistry and pre-bond surface preparation, including plasma/piranha activation and roughness control, directly correlated with bonding yield and shear strength [47].

Table 1 compares the present work with recent thin-film diamond approaches. Unlike free-standing membranes or multi-step transferred membrane schemes, our process specifically targets a true direct-bonded DOI platform on SiO_2/Si. The key distinction is a carrier-compatible route that combines sub-mm-scale photonic-grade DOI area, deep thinning to ~300 nm, preservation of the buried diamond–oxide interface, and the absence of metal or intermediate bonding layers. The resulting platform is therefore closer to a practical DOI substrate than to a released membrane demonstrator. To validate the usability of the manufactured DOI layer, we further fabricate frame-supported diamond photonic chiplets, in which waveguides are retained within a surrounding mechanical frame. This geometry provides a practical building block for heterogeneous integration of large-scale diamond quantum photonic systems.

Looking ahead, 3D integration that vertically stacks diamond qubit layers, photonics, and cryo-CMOS control electronics is regarded as a promising route to modular quantum processors and network nodes [33]. A DOI foundation layer is well suited to such stacks because it provides a planar photonic base that can co-integrate with superconducting, nonlinear, or piezoelectric films for frequency conversion and phonon-mediated interfaces, as recently explored in hybrid thin-film diamond platforms.

3. Photonic-grade DOI fabrication process

ICP-RIE is one of the most widely used approaches for thinning and structuring single-crystal diamond because it decouples plasma density and ion bombardment energy, allowing the etch rate, anisotropy, and surface modification to be tuned independently [71,75]. Early studies based on oxygen-rich plasmas established that diamond can be etched at high rates under ICP conditions, while later work showed that long oxygen-based etches often promote micromasking, nanopillar formation, and surface roughening if particles or redeposited material are present on the surface [71,76–78]. Chlorine-based plasmas, particularly Ar/Cl_2, were subsequently introduced as a complementary route because they can smooth diamond surfaces and reduce the preferential roughening frequently observed during long O_2 etches [69,72,75,79]. Therefore, more recent work has converged on cyclic processes that alternate an oxygen-rich etching step with a chlorine-based cleaning/smoothing step to combine acceptable removal rates with reduced micromasking and improved surface quality [72,75].

For directly bonded DOI substrates [47], these general considerations become more restrictive. In addition to maintaining a reasonable etch rate and a smooth diamond surface, the process must preserve the buried bonding interface and avoid exposing or damaging the underlying oxide/support stack. This is particularly important when a directly bonded diamond plate is thinned from the tens-of-micrometers range to the few-hundred-nanometer regime required for photonic-grade DOI. In the present work, the process flow therefore combines carrier-wafer engineering, gas-chemistry optimization, top-side masking, and cyclic etching. The overall route starts from a directly bonded DOI stack, then progressively modifies the carrier/support design and plasma conditions to suppress debonding and micromasking, and finally applies cyclic thinning to obtain a ~300 nm diamond film over a 0.5×0.5 mm^2 area.

The fabrication starts with a commercially available {001} surface-oriented SCD plate from ElementSix, with thickness of 300–500 μm. The

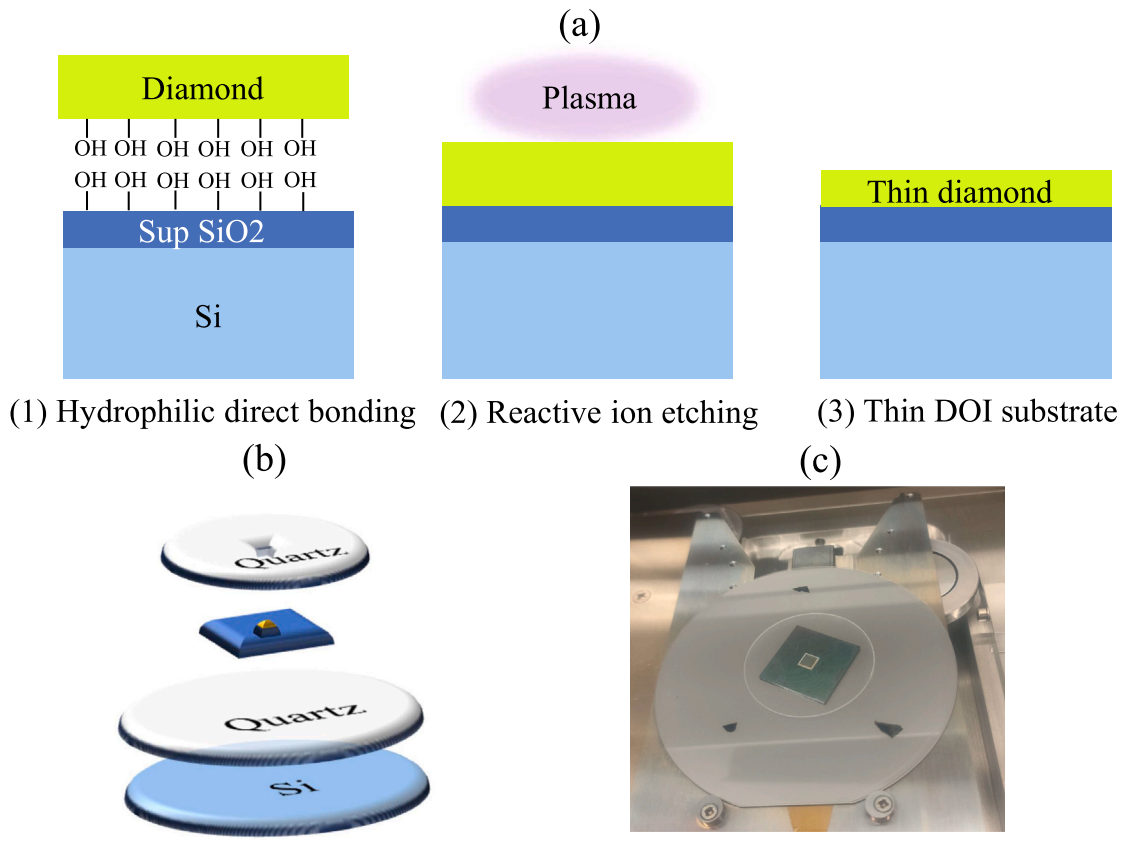


Fig. 1. (a) Schematic of the diamond thinning process. Starting with a commercial diamond plate and Si wafer, we directly bond the two plates to form the initial DOI substrate. The diamond plate thickness is then reduced by reactive ion etching, yielding a thin and smooth DOI substrate. (b) Optimized ICP-RIE carrier-wafer and mask concept. The diamond-on-insulator sample is the specimen to be etched, and a quartz mask is applied on top of the sample to minimize micromasking. The DOI substrate is mounted on a double-layer carrier-wafer stack during etching. (c) DOI sample loaded in the RIE tool (Plasmalab System 100, Oxford Instruments) for etching.

sample is then thinned to 10–20 μm by laser slicing, and polished to surface roughness of < 4 nm by soft scaife polishing (Almax easyLab), suitable for direct bonding [47]. The resulting (10-20 μm) diamond plate has a systematic thickness variation of around 1 μm over the whole area (4 × 4 mm^2). As illustrated in Fig. 1, the diamond plate is first directly bonded onto an SiO_2/Si carrier [47], forming the initial DOI structure. The bonded sample is subsequently mounted for ICP-RIE thinning using a quartz-based carrier/mask assembly designed to minimize redeposition onto the diamond surface. In the final process flow, top-side quartz masking is used to limit plasma exposure of the surrounding carrier wafer, thereby reducing the likelihood of micromasking originating from carrier erosion or redeposition. The thickness evolution of the thin diamond layer is assessed by Dektak stylus profilometry, WLI, and Raman spectroscopy, while surface quality is tracked by optical microscopy, scanning electron microscope (SEM), and atomic force microscopy (AFM). This separation between thickness metrology and surface-quality inspection proved useful throughout recipe development.

The trends in the literature summarized in Table 2 directly motivate the recipe strategy used in this work. Oxygen-rich ICP-RIE provides the required material removal rate, but long oxygen-based etches are susceptible to roughening and micro-masking-related defect formation. Ar/Cl_2, in contrast, is less suitable as the sole high-rate etch but is valuable for cleaning and smoothing [69,72]. Therefore, process development is focused on translating this established cyclic logic from free-standing membrane fabrication to directly bonded DOI substrates, where preservation of the bonding interface becomes an equally important constraint.

4. Etch recipe development for thinning bonded DOI substrates

In this section, we describe the development of a dry etching recipe for thinning down SCD bonded on SiO_2/Si substrates. As illustrated in Fig. 1(a), we started with a commercially available SCD plate (50–500 μm thick) and a silicon wafer. A 300 nm layer of SiO_2 was first deposited on the Si wafer, acting as the buried oxide layer of the DOI platform. After surface treatment of both the diamond and SiO_2/Si wafer, the two plates were directly bonded [47]. The bonded plate stack, which already formed a DOI substrate, was subsequently thinned by reactive ion etching to reduce the diamond thickness. Our goal is to fabricate a DOI substrate with a controllable thickness in the sub-micrometer range and a surface roughness below 0.5 nm, without compromising either the etch rate or the surface quality of the diamond.

A critical part of our process is dry etching, which involves preparing the carrier wafer and optimizing the etching chemistry. The carrier-wafer concept used for loading into the etch chamber is shown in Fig. 1(b). We selected quartz as both mask and carrier-wafer material wherever possible because it showed the least material redeposition during oxygen-plasma-based etching compared to other commonly used materials [69]. This became particularly important for long etch runs, where redeposition and particle accumulation can lead to severe micromasking.

4.1. Initial etching recipe and challenges

We first tested an etching sequence adapted from the process reported by Ruf et al. for producing optically coherent NV centers in micrometer-thin etched diamond membranes [69]. The corresponding

Table 2
Representative literature ICP-RIE routes relevant to DOI thinning and surface-quality control.

Study	Chemistry	Typical operating window	Main purpose	Reported outcome	Relevance here
Hwang et al. [76]	Ar/O_2	ICP 700–1000 W; bias 200 W; Ar/O_2 = 30/90 sccm	High-rate anisotropic ICP etching	Etch rate up to 40 μm/h	Illustrates why high-power oxygen-based recipes are attractive starting points for fast diamond removal
Enlund et al. [77]	Ar/O_2	2.5 mTorr; RF 600 W	Anisotropic etching of single-crystal CVD diamond	Etch rate > 200 nm/min; smooth vertical features	Shows the effectiveness of oxygen/argon ICP etching, but not its compatibility with bonded DOI
Lee et al. [79]	Ar/Cl_2	There is no optimized recipe. Recipe window: 5 mTorr; Ar/Cl_2 = 25/40 sccm; ICP coil power 100–900 W, constant ICP platen power of 300 W	Surface smoothing/isotropic chlorine-based etch	rms roughness reduced from 0.53 to 0.19 nm after 10 min	Motivates the use of Ar/Cl_2 as a cleaning/smoothing step rather than the main high-rate etch
Hicks et al. [70]	Cyclic Ar/O_2–Ar/Cl_2	Ar/O_2: 20% O_2 in Ar (50 sccm Ar), 5 mTorr, ICP power 100–200 W, platen power 300 W Ar/Cl_2: 5 mTorr, ICP power 100 W, platen power 250 W, 15 sccm Ar, 7 sccm Cl_2, Cycle: 2 min Ar/O_2 + 20 s Ar/Cl_2 cycles	Deep etching with reduced micromasking	10.6 μm depth; 45.1 nm/min; 0.47 nm rms; near-zero micromasking	Provides the key literature precedent for cyclic etching during long diamond-thinning runs
Ruf/Heupel et al. [69,72]	Alternating Ar/Cl_2 and O_2; optional soft Ar/Cl_2	Ar/Cl_2: RF/ICP = 200/500 W; O_2: 90/1100 W; soft Ar/Cl_2: 40/200 W	Membrane thinning, strain-relief etch, and roughness reduction	Quartz-supported membrane processing; low-bias Ar/Cl_2 used for additional smoothing	Provides the standard recipe family used as the initial reference point in this work

The literature table is intended to motivate the recipe-development logic rather than to provide an exhaustive recipe catalog.

Table 3
DOI substrates used for etch-recipe optimization and corresponding plasma-etch parameters.

Sample code and process step	ICP/RF (W)	Gas flow (sccm)	Pressure (μbar)	Carrier T (°C)	Duration	Result
Initial-DOI etch step 1	500/200	10 Ar/20 Cl_2	10	30	30 mins	Debonded
Initial-DOI etch step 2	1100/90	50 O_2	10	20	30 mins	Debonded
Thick-DOI gentle etch step 1	180/30	30 O_2	13	20	15 mins	Remain bonded
Thick-DOI gentle etch step 2	500/200	50 Ar/50 O_2	50	20	15 mins and 60 mins	Remain bonded
DOI-quartz etch step 1	1000/90	50 O_2	10	20	15 mins	Remain bonded
DOI-quartz etch step 2	500/200	10 Ar/20 Cl_2	10	30	20 mins	Remain bonded

parameters are listed in Table 3 as the "Initial-DOI etch". In our case, the starting substrate was a 4 mm × 4 mm single-crystal diamond plate directly bonded to a 300 nm PECVD SiO_2 layer on a Si handle wafer. In the reference process, the Ar/Cl_2 plasma is used primarily as a surface-cleaning step to remove particles and suppress micromasking, whereas the O_2 plasma provides the main diamond-removal step. However, when these relatively high-power plasma conditions were applied to the directly bonded DOI samples, debonding occurred during both the Ar/Cl_2 and O_2 steps. The debonding was identified optically from the appearance of interference fringes after etching, consistent with the formation of an air gap at the diamond–oxide bonding interface.

Two possible mechanisms were considered for the observed debonding. The first was a lateral attack or under-etching of the buried SiO_2 layer. Because the Ar/Cl_2 plasma can have an isotropic component and parts of the surrounding carrier surface may be exposed during etching, the buried oxide could, in principle, be attacked from the diamond edges. However, for a 4 mm × 4 mm bonded diamond plate, complete removal of the oxide underneath the diamond by lateral etching alone is unlikely over the time scale of the process. In addition, debonding was also observed during the O_2 etching step, where chemical removal of SiO_2 is not expected to be the dominant process. We therefore considered oxide under-etching to be insufficient by itself to explain the observed failure.

The second and more plausible mechanism would be plasma-induced thermomechanical stress. Under high-power plasma conditions, the Si handle wafer can experience stronger heating and a larger thermomechanical response than the bonded diamond layer. This mismatch can generate interfacial stress and trigger local bond failure, especially when the buried oxide is only 300 nm thick and therefore cannot substantially accommodate the difference in expansion between the diamond and the Si carrier. Representative room-temperature thermal expansion coefficients are approximately 1.0–1.1 ppm K^{-1} for diamond and 2.6 ppm K^{-1} for single-crystal silicon, with the latter increasing further at elevated temperature [9,80,81]. This difference provides a credible route for plasma-induced interfacial stress during rapid heating and cooling.

To distinguish between these mechanisms, we prepared DOI samples with three controlled variations: SiO_2 thickness, SiO_2 deposition method, and carrier substrate material. Increasing the SiO_2 thickness reduces the likelihood that the buried oxide is fully removed by lateral attack from the edges, and is also advantageous for the later release of free-standing photonic structures. We compared PECVD and thermally grown SiO_2 because thick PECVD oxide can introduce higher surface roughness, which may complicate direct bonding, whereas thermally grown SiO_2 can provide micrometer-scale oxide thickness with high surface quality. Finally, fused quartz was introduced as an alternative carrier substrate to test the thermal-shock hypothesis. Its thermal expansion coefficient, approximately 0.5–0.55 ppm K^{-1}, is much closer to that of diamond than silicon [9,80,81], making quartz a useful platform for testing the thermal-shock hypothesis.

4.2. Low-power etching using diamonds bonded to thick PECVD/thermal oxide

To reduce the risk of complete oxide loss during plasma processing, we increased the SiO_2 thickness from 300 nm to 2.5 μm using PECVD (Rq=4.44 nm). Using this thick-oxide DOI substrate, we tested modified

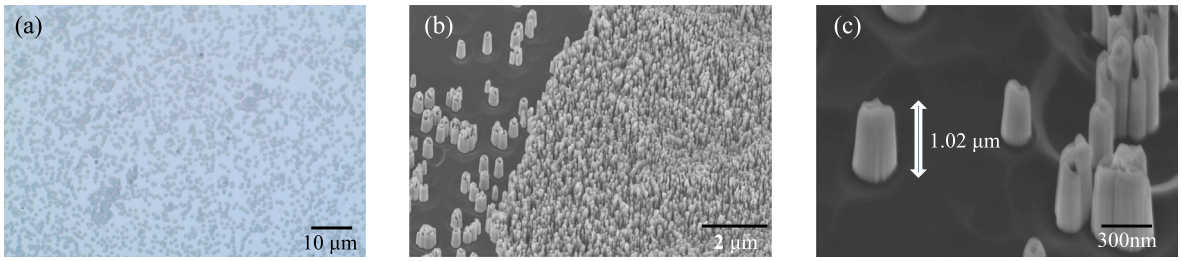


Fig. 2. Observed surface damage after long etching with initial DOI etching recipe, without quartz mask. (a) optical microscope image of the surface. (b) Top-view SEM image of the diamond surface after extended etching, showing nanopillar-like structures associated with micromasking. (c) A nanopillar with a height of 1.04 µm, imaged at 60k magnification. The sample carrier was tilted by 15°.

etching conditions with reduced ICP/RF power, and therefore lower thermal loading, as summarized in Table 3.

Thick-DOI gentle etch step 1 was a low-power version of the initial O_2-based diamond etch. After 15 min of processing, the diamond plate remained bonded, confirming that reducing the plasma load can mitigate the debonding observed under the initial high-power conditions. However, the reduced power also lowered the material-removal rate, making this condition insufficient by itself for practical DOI thinning. We therefore tested an oxygen-rich Ar/O_2 chemistry, denoted as Thick-DOI gentle etch step 2 in Table 3, where Ar was added to the O_2 plasma to increase the effective removal rate while avoiding the original high-power O_2 condition. The diamond remained bonded after 15 min of etching. The same Ar/O_2 recipe was then applied for an extended duration to a diamond plate bonded to 2.5 µm thermally grown SiO_2 on Si (Rq=0.2 nm), where the bonding interface was preserved even after 60 min of etching. These results show that Si-based DOI carriers can withstand extended diamond thinning when the plasma conditions are moderated.

Although the bonding was preserved, the surface quality after the extended Ar/O_2 etch was not suitable for photonic-grade DOI. Optical microscope and SEM inspections were therefore used to identify the origin of the roughening. As shown in Fig. 2a, the top-view optical microscope image reveals a high density of surface defects. After tilting the sample holder by 15°, SEM inspection, shown in Fig. 2b,c, reveals a dense pillar-like morphology. These features are characteristic of micromasking-driven roughening, where local particles, residues or redeposited material partially shield the diamond during oxygen-based etching and lead to the formation of nanopillars or pits [69,70]. This observation is important for the process development: reducing the plasma power can preserve the direct-bonded DOI interface, but power reduction alone does not provide the surface quality required for photonic applications.

4.3. High-power etching of diamond bonded to quartz carriers

The moderated etching experiments on Si-based carriers showed that the bonding interface can be preserved once the plasma load is reduced, suggesting that complete under-etching of the buried oxide is unlikely to be the dominant cause of debonding. To directly test the role of thermomechanical mismatch, we prepared an additional DOI substrate by bonding diamond to a 300 nm PECVD SiO_2 layer on a fused-quartz carrier. Fused quartz was selected because its thermal expansion coefficient is much closer to that of diamond than silicon, making it a useful diagnostic substrate for testing the thermal-shock hypothesis [81,82].

After successful bonding, the quartz-based DOI substrate was etched using the original high-power reference conditions listed in Table 3, i.e., the same conditions that caused debonding on Si-based carriers. The sample remained bonded after both the 15 min O_2 etch and the subsequent 20 min Ar/Cl_2 step. This result strongly supports thermal expansion mismatch as the main origin of the debonding observed for diamond bonded to SiO_2/Si. At the same time, the quartz experiment also showed that bond survival alone is not sufficient for photonic-grade DOI thinning: severe micromasking was still observed after etching. Thus, the quartz carrier resolves the debonding problem in a diagnostic sense, but does not by itself provide a manufacturable route for DOI thinning on a conventional Si platform.

4.4. Origin of particle-induced micromasking and process implications

After resolving the debonding issue, micromasking-induced surface degradation became the remaining critical limitation for achieving photonic-grade DOI thinning. The responsible particles can originate from two routes. First, they may already be present on the diamond surface due to growth, polishing, handling, cleaning residues, or external contamination. Second, they may be generated during plasma processing when exposed regions of the surrounding carrier wafer or mask stack are etched and redeposited onto the diamond surface. During oxygen-based diamond etching, such local micromasks partially protect the underlying diamond and evolve into nanopillars or pits, as also reported for etched diamond membranes [69,70].

These observations led to two process changes. First, a fused-quartz top mask with a laser-cut opening was introduced to limit direct plasma exposure of the surrounding carrier surface and reduce redeposition-driven micromasking. Second, the Ar/Cl_2 cleaning step was incorporated cyclically rather than used only as a pre-etch. In this way, newly accumulated particles can be removed during long etches before they develop into large surface defects. Together with reduced handling time between cleaning, bonding, mounting, and etching, these changes define the process requirements for a manufacturable DOI-thinning route: the recipe must preserve the bonded interface while repeatedly refreshing the diamond surface during material removal.

5. Final optimized cyclic recipe and manufactured photonic-grade DOI substrate

5.1. Etch parameters

The recipe-development study above shows that a successful DOI-thinning process must satisfy three requirements simultaneously: the bonding interface must survive plasma exposure, carrier-induced redeposition must be minimized, and the diamond surface must be repeatedly cleaned during long etch runs. The final recipe developed in this work, therefore, combines moderated plasma conditions, carrier/mask engineering, and cyclic etching. In contrast to the initial high-power reference process, the main removal step is implemented using an Ar/O_2 plasma rather than pure O_2, while the Ar/Cl_2 plasma is retained as a dedicated cleaning and smoothing step. In addition, the carrier and mask configuration is designed to limit unnecessary exposure of the surrounding wafer surface, thereby reducing redeposition-driven micromasking.

The optimized cyclic recipe is summarized in Table 4. One full cycle consists of a 4 min Ar/Cl_2 step followed by a 4 min Ar/O_2 step.

Table 4
Optimized cyclic etching recipe developed in this work. One full cycle consists of 4 min Ar/Cl_2 followed by 4 min Ar/O_2.

Parameter	Ar/Cl_2	Ar/O_2
ICP (W)	100	200
RF (W)	250	300
Gas flow (sccm)	Ar 15/Cl_2 7	Ar 50/O_2 13
Chamber pressure	0.01 mbar	0.01 mbar
Carrier temperature	20 °C	20 °C
Diamond etch rate (nm/min)	~10	~50–55
Step duration	4 min	4 min

The Ar/Cl_2 step is used primarily for cleaning/smoothing, while the Ar/O_2 step provides the main material removal.

The Ar/Cl_2 step primarily removes surface particulates and smooths the diamond surface, with an etch rate of approximately 10 nm/min under the selected conditions. The Ar/O_2 step provides the main diamond removal, with an etch rate of approximately 50–55 nm/min. Both steps are carried out at a chamber pressure of 0.01 mbar and a carrier temperature of 20 °C. Repeated execution of this 4 min + 4 min cycle enabled stable thinning of directly bonded diamond plates from the 10–20 μm range down to the photonic-grade regime. In the DOI demonstration reported here, a 10 μm bonded diamond plate was thinned to ~300 nm over an area of 0.5×0.5 mm^2 while preserving the buried diamond–oxide interface. This optimized recipe completes the etch-development storyline. The earlier experiments showed that high-power reference recipes can trigger debonding on Si-based DOI, that lowering the plasma load preserves the bond but does not by itself suppress micromasking, and that quartz support confirms the role of thermal shock while also highlighting the need for improved particle control. The final cyclic Ar/Cl_2 + Ar/O_2 process addresses these issues together and is therefore used for the DOI substrates presented in the remainder of this work.

5.2. Photonic-grade DOI substrate

Using the optimized cyclic recipe, we achieved controlled thinning of a direct-bonded DOI substrate to the photonic-grade thickness range. Fig. 3 summarizes the characterization of the resulting thin film. The fabricated DOI contains a 0.5 mm×0.5 mm region with a target thickness of approximately 300 nm. We use the particle on top left of Fig. 3a to localize the target area. As shown in Fig. 3b, the orange square marks the region reaching the target ~300 nm thickness (verified by WLI measurements as shown in Fig. 3f, 1D thickness profile data of two representative lines-horizontal (line 1) and vertical (line 2) are detailed in Fig. 3 g and h, respectively), while the surrounding bonded diamond remains thicker, up to approximately 1 μm. This spatial thickness profile arises from the mask-defined plasma exposure during etching and the initial thickness variation of the starting diamond plate. The target thin-film region is largely free of visible contaminants and micromasking-induced structures, confirmed by SEM images in Fig. 3a. Surface characterization shows a roughness of $R_q < 0.5$ nm, shown in Fig. 3d, indicating that the cyclic cleaning/etching strategy can preserve photonic-grade surface quality during deep thinning. We observe a $\sim 50 - 70$ nm thickness variation across the 0.5×0.5 mm^2 photonic-grade DOI area, which arises from the quartz mask-related etch non-uniformity and the initial thickness variation of the starting diamond plate. Importantly, the buried diamond–oxide interface remained intact after thinning, confirming that the optimized process can combine aggressive material removal with bond preservation and surface-quality control.

5.3. Summary of etch process optimization

The recipe-development study leads to three main conclusions. First, the debonding observed with the original high-power reference recipes on directly bonded SiO_2/Si DOI is primarily associated with thermomechanical shock rather than complete under-etching of the buried oxide. This conclusion is supported by the survival of thick-oxide Si-based samples during moderated etching and by the successful high-power etching of diamond bonded to quartz. Second, preserving the bonding interface alone is not sufficient for photonic-grade DOI fabrication: long oxygen-rich etches can produce severe micromasking, nanopillars, and unacceptable roughening unless particle generation and redeposition are actively controlled. Third, a practical DOI-thinning process must combine moderated plasma conditions, carrier/mask engineering, and cyclic surface cleaning.

Taken together, these findings define the optimized process used in this work: a quartz-assisted carrier/mask configuration combined with a 4 min Ar/Cl_2 + 4 min Ar/O_2 cyclic ICP-RIE recipe. The Ar/Cl_2 step repeatedly refreshes the surface by removing particulates and smoothing the diamond, while the Ar/O_2 step provides the etch rate required for efficient thinning. With this combined strategy, bonded SCD plates in the 10–20 μm range can be thinned to the photonic-grade regime. In the demonstrated process, a 10 μm bonded plate was reduced to a ~300 nm DOI film over 0.5×0.5 mm^2 while preserving the buried interface and maintaining sub-nanometer surface roughness. This optimized cyclic recipe therefore provides the process foundation for the photonic-grade DOI substrates, chiplet fabrication, and thickness-validation results presented in the following sections.

6. Diamond anisotropic etch recipe optimization for photonic chiplet fabrication from DOI substrate

Device fabrication was carried out on the photonic-grade DOI substrate obtained in the previous section, consisting of a sub-μm-thick diamond layer bonded to a SiO_2/Si carrier wafer. The main fabrication steps are schematically illustrated in Fig. 4. The substrate (step 1) was first cleaned by rinsing in acetone and isopropanol (IPA). In step (2), a SiN hard mask was then deposited by PECVD, followed by spin coating of AR-P-6200.09 (CSAR62) electron-beam resist. The chiplet pattern was defined in CSAR62 by electron-beam lithography and resist development, and subsequently transferred into the SiN hard mask using a CHF_3/O_2-based RIE (step 3) [69,83]. An oxygen-based anisotropic dry etch was then used to transfer the pattern into the diamond layer in step (4). Finally, in step (5) buffered oxide etchant (BOE, 7:1 v/v mixture of 40 wt% NH_4F and 49 wt% HF) at room temperature was used to remove the SiN mask and undercut the buried SiO_2. The sample was subsequently dried using critical point drying (CPD), thereby releasing the free-standing diamond structures from the DOI substrate.

6.1. Anisotropic diamond etch on DOI substrate

To transfer patterns from the SiN hard mask to the diamond substrate, a high-accuracy, top-down, anisotropic diamond etch process is required. For photonic device fabrication based on DOI substrate, two additional requirements must be satisfied. First, micro-masking during diamond etch must be addressed to ensure a smooth device surface. Second, the bonding interface must be preserved with high quality throughout the ICP-RIE process, which is also beneficial for the subsequent HF-based undercut step.

We first evaluated the cyclic diamond thinning-down recipe developed in Section 4 which provides efficient anisotropic diamond etch while maintaining good surface quality and preserving the bonding interface. However, the recipe was optimized for anisotropic diamond etch using a quartz mask and was not directly compatible with pattern transfer using a SiN hard mask. The use of a SiN hard mask will cause micro-masking resulted from SiN material re-deposition during the Ar-atoms contained etch process. Therefore, a dedicated anisotropic diamond etch recipe had to be developed separately for pattern transfer from the SiN hard mask into the diamond substrate.

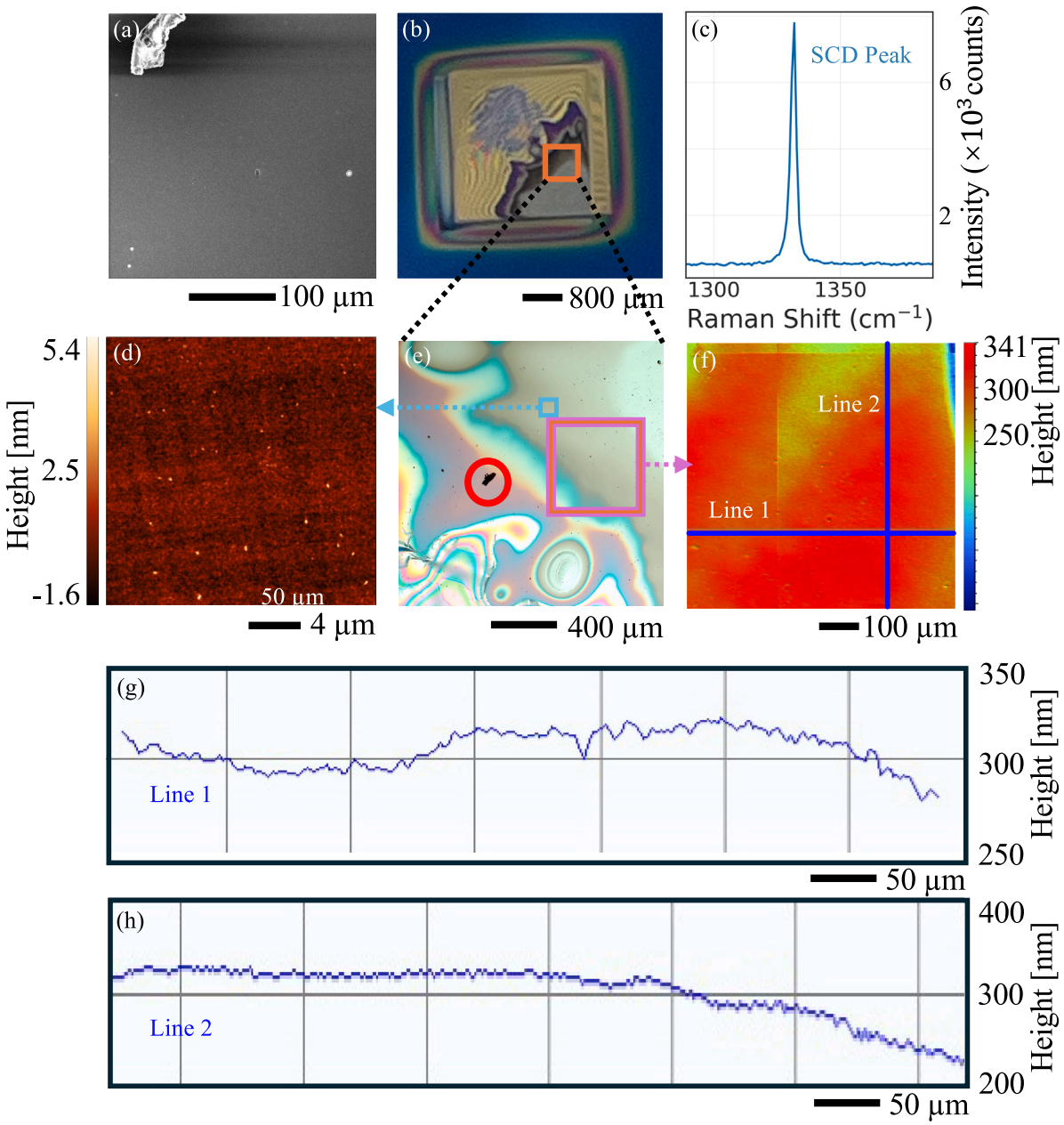


Fig. 3. Overall characterization of the fabricated DOI thin film. (a) SEM image at ×300 magnification. Sample surface does not have many visible contaminants, even though we did not keep the entire etching/handling/inspection very clean. The large particle on the top right is used as a marker to localize the target area, for example, as the black dot in the red circle of subfigure (e). (b) Optical microscopy image of the entire DOI substrate, where the orange square indicates the target 0.5 mm × 0.5 mm region. (c) Raman spectrum from the target area which confirms the presence of SCD. (d) Representative AFM topography showing a roughness R_q of < 0.5 nm. (e) Zoomed-in optical microscopy image, and the color contrast corresponds to thickness variations, with the purple region is the target region. (f) WLI image of the target thin film. Thickness profiles were extracted along a horizontal line (line 1 in (g)) and a vertical line (line 2 in (h)), both indicating an average thickness of approximately 300 nm.

As an alternative starting point, we investigated a pure oxygen-plasma-based etching process [6] with etch parameters listed in Table 3 "Initial-DOI etch 1". This etch process has shown highly anisotropic diamond etch, absence of micro-masking, and smooth sidewall of our target 200–300 nm device thickness range. However, the thermal-shock issue described in Section 4 reappeared, even for etch durations of only several tens of seconds.

Based on the experience from these two processes, we developed a new cyclic diamond etch recipe tailored for top-down pattern transfer using a SiN hard mask. The recipe was designed to mitigate both thermal shock and micro-masking with a few key characteristics. First, a cyclic etch method is designed without heavy Ar ions and with reduced plasma power. Etch cycle loop consists of a 15 s O_2 etch step (50 sccm O_2, 10 µbar chamber pressure) using an RF power of 300 W and an ICP power of 200 W on Oxford Instruments Plasmalab System 100 RIE system. The etch step is followed by a 5 min cooling step. Second, the carrier-wafer table temperature was reduced from 20 °C to 0 °C to compensate for the heating induced by the high-power plasma. Third, the helium backside-cooling flow was increased from 5 sccm to 10 sccm to improve thermal contact between the DOI substrate and the carrier-wafer table.

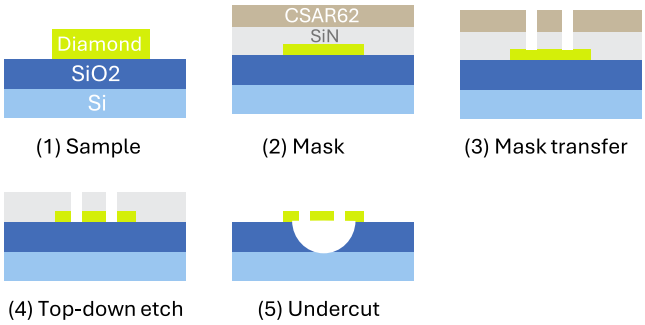


Fig. 4. DOI based fabrication process. Sample is prepared from previous stage where sub-μm thin diamond is directly bonded onto SiO_2/Si substrate via chemical bonds. Pattern is defined by E-beam lithography and transferred via a SiN hard mask. HF undercut is used lastly for free-standing structures. More details can be found in the main text.

6.2. Photonic chiplets from DOI substrate

Using the optimized etch recipes and process flow, we fabricated free-standing diamond photonic chiplets consisting of waveguides retained within a surrounding support frame, as shown in Fig. 5a,b. The frame provides mechanical robustness during release and handling, while the internal waveguide structures form the photonic element intended for heterogeneous integration. The suspension of the chiplet is confirmed by dark-field microscopy and by pick-and-place manipulation, as shown in Fig. 5c,d. In this test, a diamond chiplet is picked up with a probe through van der Waals adhesion, demonstrating compatibility with subsequent transfer onto a photonic integrated circuit receptor for hybrid photonic integration [34,84].

A higher-magnification SEM image of the waveguide cross section, shown in the inset of Fig. 5b, confirms that the waveguides are fully released and that no residual support pedestal remains underneath the structures. This is an important practical advantage of the DOI-based release process.

Here, we demonstrate a full-stack fabrication flow for a photonic-grade DOI substrate. Using this platform, we fabricate free-standing diamond photonic chiplets, while the same DOI approach also enables complex, non-suspended diamond photonic circuits directly supported by the oxide layer.

7. Contrast and thickness evaluation of diamond layer on SiO_2

Under visible illumination, a DOI stack exhibits thickness-dependent colors due to thin-film interference in the diamond and SiO_2 layers. This effect can be used as a simple and rapid optical indicator of diamond thickness during thinning, similar to the optical-contrast methods widely used for graphene and other thin-layer systems on SiO_2/Si substrates [85–87]. We model the DOI system as a four-layer stack composed of air, diamond, SiO_2, and Si, as schematically shown in Fig. 6a. The refractive indices are denoted as $n_0 = 1$ for air, $n_1 = 2.41$ for diamond [88], $n_2 = 1.46$ for SiO_2 [89,90], and $n_3 = 4$ for Si [91]. The diamond thickness d_1 is varied from 0 to 1200 nm, while the SiO_2 thickness d_2 is varied from 0 to 600 nm. For this first-order contrast model, the refractive indices are taken at $\lambda = 550$ nm and treated as constant across the visible range. This approximation captures the main interference-driven thickness dependence near the green channel of an optical microscope; full color rendering can be obtained by extending the same transfer-matrix calculation over the visible spectrum with wavelength-dependent optical constants.

At normal incidence, the intensity reflectance of the DOI stack is calculated from the Fresnel coefficients and phase accumulation in the diamond and SiO_2 layers. Following the multilayer interference formalism used for thin-film visibility calculations [87], the reflectance of the air/diamond/SiO_2/Si stack is written as

$$R_{\mathrm{Dia}} = \left| \frac{r_1 e^{i(\phi_1+\phi_2)} + r_2 e^{-i(\phi_1-\phi_2)} + r_3 e^{-i(\phi_1+\phi_2)} + r_1 r_2 r_3 e^{i(\phi_1-\phi_2)}}{e^{i(\phi_1+\phi_2)} + r_1 r_2 e^{-i(\phi_1-\phi_2)} + r_1 r_3 e^{-i(\phi_1+\phi_2)} + r_2 r_3 e^{i(\phi_1-\phi_2)}} \right|^2, \quad (1)$$

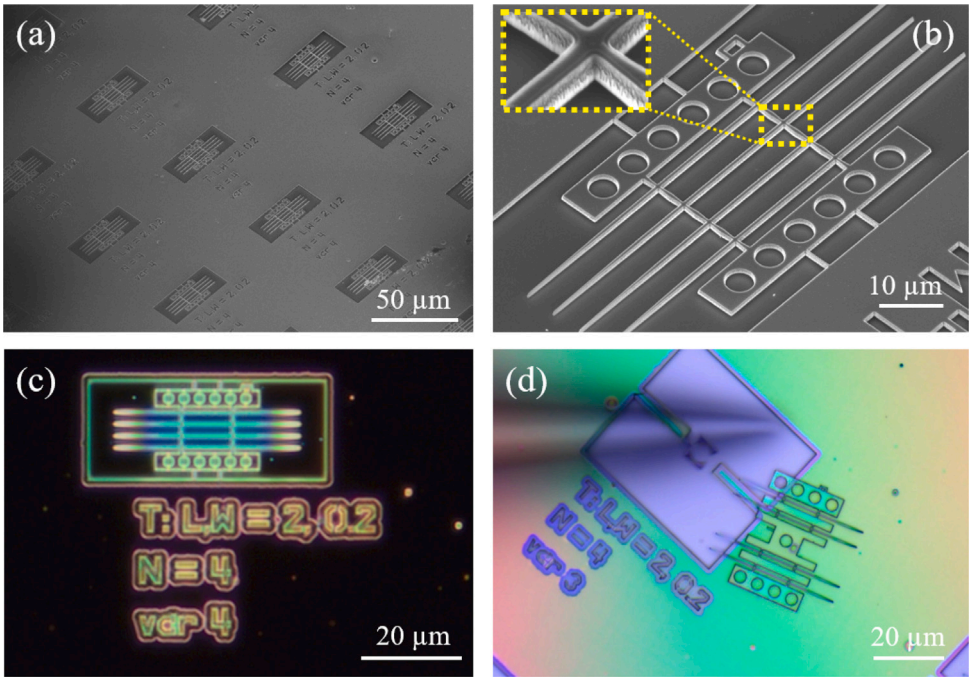


Fig. 5. SEM and microscope inspection of fabricated chiplets. (a) Zoomed-out view of fabricated chiplets aray. (b) Zoomed-in image of a single chiplet. The tether structure and waveguides are fabricated successfully and connected by a supporting frame. The smooth top surface indicates low roughness after the whole frabrication process. The top-left inset image shows no pole structure underneath the crosses. (c) Dark-field optical microscope image of a chiplet together with (d) where a chiplet is picked up by a needle via van der Waals force indicate the successful undercut.

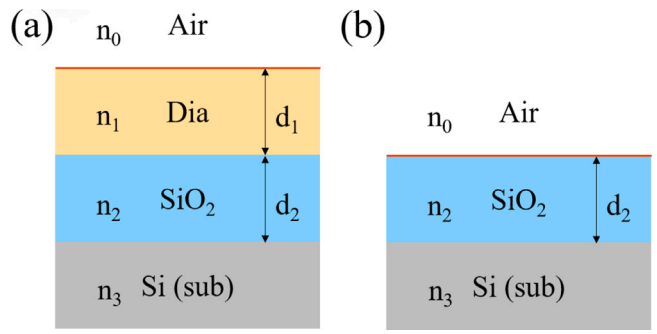


Fig. 6. (a) Trilayer scheme of diamond on SiO_2 / Si substrate and (b) bilayer scheme of the SiO_2 / Si substrate.

where

$$r_1 = \frac{n_0 - n_1}{n_0 + n_1}, \qquad r_2 = \frac{n_1 - n_2}{n_1 + n_2}, \qquad r_3 = \frac{n_2 - n_3}{n_2 + n_3}, \tag{2}$$

and

$$\phi_i = \frac{2\pi n_i d_i}{\lambda} \tag{3}$$

is the phase accumulated in layer i for wavelength λ.

For comparison, the reflectance of the bare SiO_2/Si substrate, shown schematically in Fig. 6b, is obtained by setting the diamond layer thickness to zero. The corresponding expression is

$$R_{\mathrm{Sub}} = \left| \frac{r_2' e^{i\phi_2} + r_3 e^{-i\phi_2}}{e^{i\phi_2} + r_2' r_3 e^{-i\phi_2}} \right|^2, \tag{4}$$

where

$$r_2' = \frac{n_0 - n_2}{n_0 + n_2}. \tag{5}$$

The optical contrast of a diamond film relative to a reference region can then be defined as the relative change in reflected intensity,

$$C(\lambda) = \left| \frac{R_{\mathrm{Dia}}(\lambda) - R_{\mathrm{ref}}(\lambda)}{R_{\mathrm{Dia}}(\lambda)} \right|, \tag{6}$$

where R_{ref} can be either the reflectance of the bare SiO_2/Si substrate, R_{Sub}, or the reflectance of a diamond region with a known reference thickness. This contrast definition provides a direct way to identify thickness ranges with high optical visibility and to select suitable SiO_2 thicknesses for microscope-based thickness evaluation. In the following analysis, we use this interference model to calculate the expected color and contrast evolution of DOI stacks and then correlate the calculated trends with optical micrographs and white-light interferometry measurements.

7.1. Contrast of diamond for single wavelength

As shown by the reflectance expressions above, the optical contrast of a DOI stack depends on the thicknesses and refractive indices of the constituent layers, as well as on the illumination wavelength. In Fig. 7a, the SiO_2 thickness is varied from 0 to 600 nm while the contrast is calculated between diamond layers of 300 and 305 nm thickness. In this case, the contrast shows a pronounced modulation with broader spacing between maxima. A comparable trend is observed in Fig. 7b, where a 300 nm diamond layer is placed on SiO_2 layers differing by 5 nm in thickness.

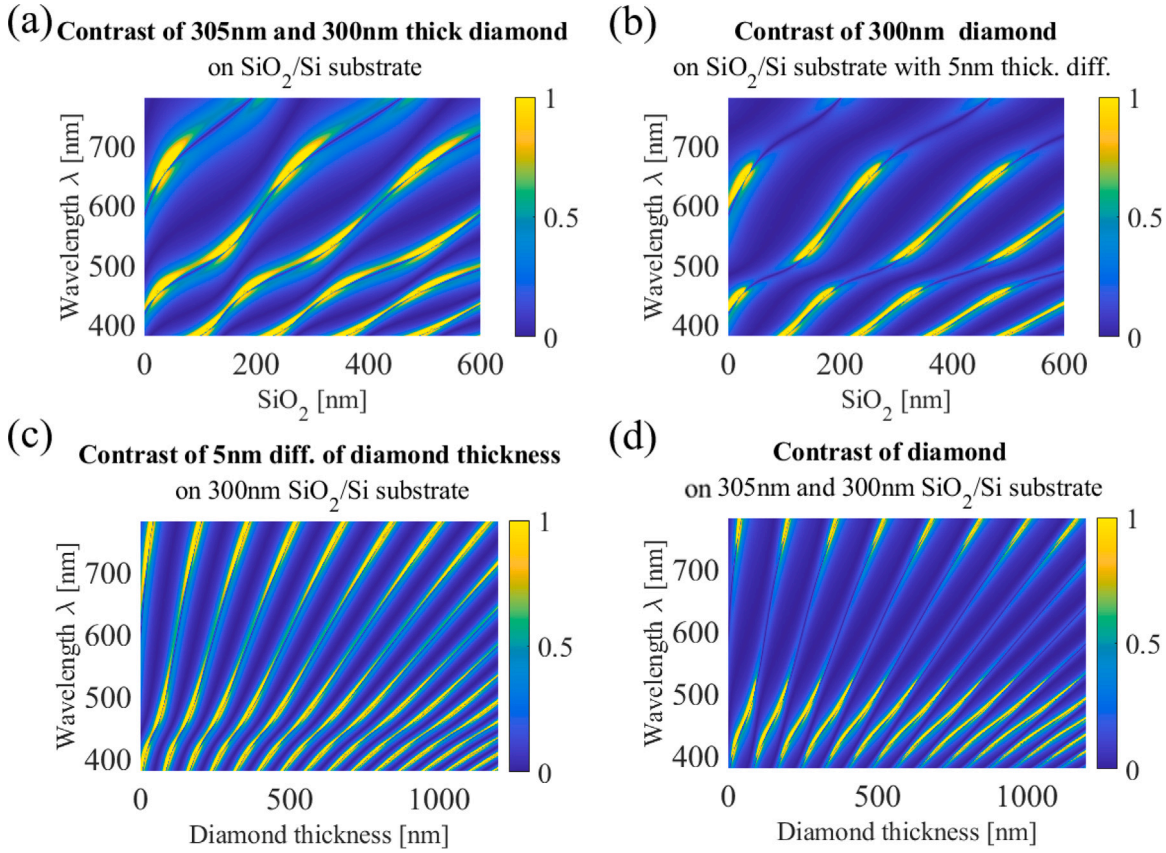


Fig. 7. Contrast between (a) diamond layers with 305 nm and 300 nm thickness on SiO_2/Si with thickness of SiO_2 varying from 0 to 600 nm, (b) 300 nm thick diamond layers on varying SiO_2/Si substrates differing of 5 nm SiO_2 thickness, (c) diamond layers differing of 5 nm thickness on a 300 nm SiO_2/Si substrate for diamond thicknesses varying from 0 to 1 μm (d) diamond layers of the same thickness on 305 nm and 300 nm SiO_2/Si substrates for diamond thicknesses varying from 0 to 1 μm.

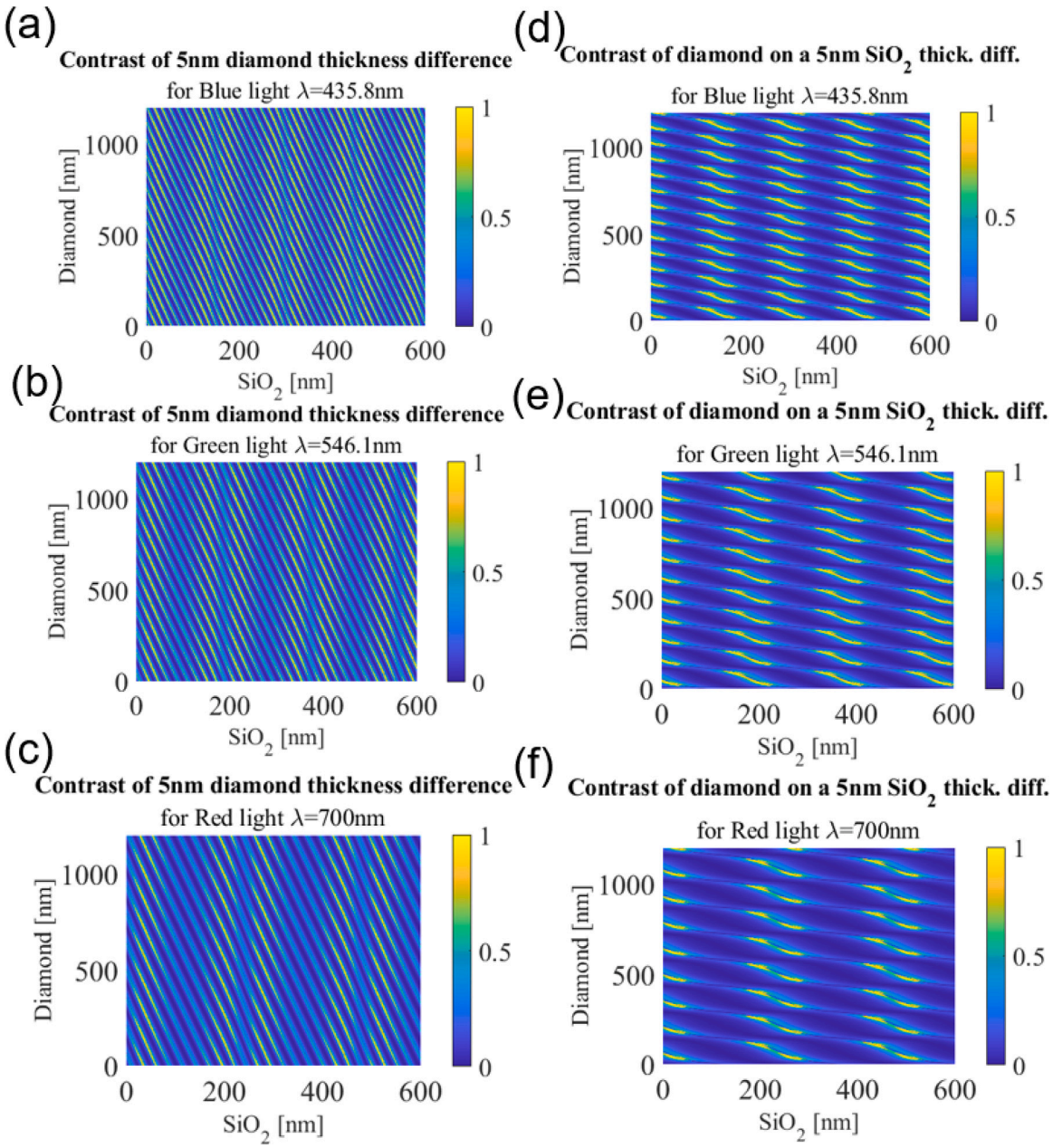


Fig. 8. Contrast of diamond layers with 5 nm thickness difference on SiO_2 substrate for monochromatic (a) blue, (b) green, and (c) red light; contrast of diamond on SiO_2 substrate with 5 nm thickness difference for monochromatic (d) blue, (e) green, and (f) red light.

Fig. 7c shows the calculated contrast between a diamond layer of thickness d and a layer 5 nm thicker, both on a 300 nm SiO_2/Si substrate, for wavelengths in the visible range (380–780 nm) and diamond thicknesses from 0 to 1200 nm. For a fixed wavelength, the contrast exhibits a series of maxima. These maxima are approximately periodic in diamond thickness, and their spacing increases with wavelength, as expected from the phase accumulation in the diamond film. A similar behavior is obtained when the oxide thickness is varied. Fig. 7d shows the contrast between two otherwise identical DOI stacks in which the SiO_2 thicknesses are 300 and 305 nm, respectively. The resulting pattern is qualitatively similar to that in Fig. 7c, indicating that small changes in either the diamond or oxide thickness can produce measurable changes in optical contrast.

The maxima in Fig. 7 identify thickness and wavelength combinations for which small changes in diamond or SiO_2 thickness produce the largest optical response. These conditions therefore provide useful guidance for selecting oxide thicknesses and illumination wavelengths for thickness evaluation. Physically, the maxima arise from coupled thin-film interference in the diamond and SiO_2 layers. The SiO_2 layer is bounded by higher-index media in the DOI stack, whereas the diamond layer is bounded by lower-index media at the air/diamond and diamond/SiO_2 interfaces. The resulting phase conditions act as coupled Fabry–Pérot-like resonances that enhance the sensitivity of reflectance to small thickness variations. Fig. 8 shows the contrast as a function of diamond and SiO_2 thickness under monochromatic blue (λ = 435.8 nm), green (λ = 546.1 nm), and red (λ = 700 nm) illumination. In Fig. 8a–c, the contrast is calculated between diamond layers differing by 5 nm. Two families of contrast maxima are visible, corresponding to the interference conditions associated with the diamond and SiO_2 layers. The spacing between these features increases with wavelength. A similar pattern of overlapping maxima is observed in Fig. 8d–f, where the compared systems differ by 5 nm in SiO_2 thickness while the diamond thickness is kept fixed. These calculations show that both diamond and oxide thickness variations can be detected optically, but

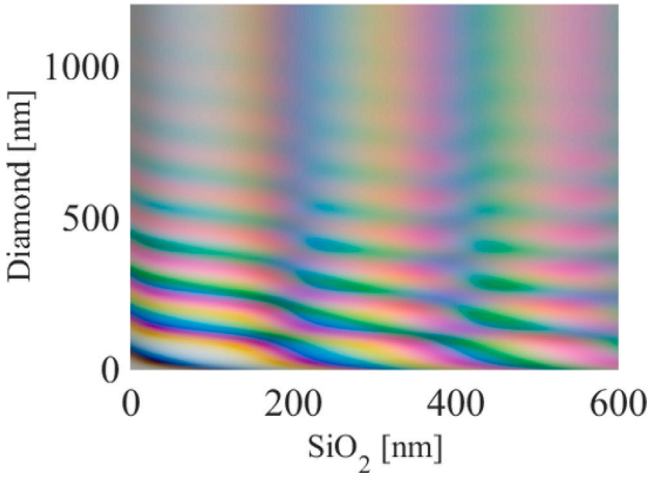


Fig. 9. Color map of diamond on a SiO_2/Si substrate for assuming a brightness of 100%.

that sensitivity depends strongly on wavelength and local position in the DOI thickness map.

7.2. Contrast of diamond in the visible spectrum

The single-wavelength analysis is directly relevant for filtered or monochromatic illumination. However, optical microscope images acquired under standard white-light conditions contain contributions from the full visible spectrum. To describe the perceived color of the DOI stack, we used the colorimetric CIE 1931 XYZ space [92] and calculated the XYZ tristimulus values as

$$\begin{pmatrix} X \\ Y \\ Z \end{pmatrix} = P \int_{380\ \mathrm{nm}}^{780\ \mathrm{nm}} S(\lambda)R(\lambda) \begin{pmatrix} \bar{x}(\lambda) \\ \bar{y}(\lambda) \\ \bar{z}(\lambda) \end{pmatrix} d\lambda, \tag{7}$$

where $\bar{x}(\lambda)$, $\bar{y}(\lambda)$, and $\bar{z}(\lambda)$ are the CIE 1931 color-matching functions tabulated in Ref. [92], $R(\lambda)$ is the calculated reflectance of the DOI stack, and $S(\lambda)$ is the spectral power distribution of the illumination source. For the microscope illumination used here, the source is approximated by CIE Illuminant A, corresponding to a tungsten-filament source with a color temperature of approximately 2856 K. The prefactor P accounts for the overall intensity normalization.

The calculated XYZ values can be converted to RGB using standard color-space transformations, followed by display-specific corrections such as gamma correction for sRGB or AdobeRGB. This procedure produces a simulated color map of the DOI stack from its calculated reflectance spectrum. Fig. 9 shows such a color map for diamond thicknesses from 0 to 1200 nm and SiO_2 thicknesses from 0 to 600 nm, displayed in the sRGB color space for brightness of 100% or P = 1. Changing P changes the calculated luminance and therefore the displayed brightness; in the absence of clipping or display nonlinearities, the chromaticity is preserved. The color map shows that the DOI stack provides strong thickness-dependent color contrast, especially for thinner diamond and SiO_2 layers. Although the color response is not globally one-to-one because thin-film interference is periodic, sufficiently distinct color regions can be used for rapid thickness estimation when combined with an appropriate calibration.

For a quantitative comparison between two colors, it is useful to transform the XYZ values into the CIE 1976 $L^*a^*b^*$ color space, which is more perceptually uniform than RGB or XYZ [92,93]. The CIELAB coordinates are obtained from

$$L^* = 116 f\left(\frac{Y}{Y_n}\right) - 16,$$

$$a^* = 500\left[f\left(\frac{X}{X_n}\right) - f\left(\frac{Y}{Y_n}\right)\right], \tag{8}$$

$$b^* = 200\left[f\left(\frac{Y}{Y_n}\right) - f\left(\frac{Z}{Z_n}\right)\right],$$

where X_n, Y_n, and Z_n are the tristimulus values of the reference white point. For Illuminant A and the CIE 1931 2° standard observer, these values are X_n = 109.850, Y_n = 100, and Z_n = 35.585. The function $f(t)$ is defined as

$$f(t) = \begin{cases} t^{1/3}, & \text{if } t > \left(\frac{6}{29}\right)^3, \\ \frac{1}{3}\left(\frac{29}{6}\right)^2 t + \frac{4}{29}, & \text{otherwise.} \end{cases} \tag{9}$$

In this space, L^* represents perceptual lightness, from 0 for black to 100 for white, while a^* represents the green–red axis and b^* represents the blue–yellow axis. Unlike RGB-based color spaces, CIELAB is device independent once the illuminant and reference white point are specified. It is therefore better suited for comparing colors generated by different DOI thicknesses.

The total color difference (TCD), expressed here using the CIE76 color-difference metric ΔE^*_{ab}, quantifies the perceptual distance between two reflected colors in the CIE $L^*a^*b^*$ color space. The TCD is then calculated using the CIE76 Euclidean distance,

$$TCD_{\mathrm{CIE76}} = \sqrt{(\Delta L^*)^2 + (\Delta a^*)^2 + (\Delta b^*)^2}. \tag{10}$$

This metric provides a simple quantitative measure of perceptual color separation between two DOI stacks. Fig. 10a shows the total color difference between two systems whose diamond thicknesses differ by 5 nm, while Fig. 10b shows the corresponding result for a 5 nm difference in SiO_2 thickness. The TCD map in Fig. 10a follows the main color variations visible in Fig. 9, confirming that CIELAB distance is a useful metric for identifying thickness regions with high optical sensitivity. Fig. 10b shows additional modulation features associated with the oxide-layer interference. A full quantitative interpretation of these secondary features is beyond the scope of this work; here, the TCD analysis is used primarily as a practical guide for selecting DOI thickness ranges that provide strong color sensitivity for microscope-based thickness evaluation.

7.3. Algorithm for the thickness evaluation of diamond layer on SiO_2

Based on the above considerations, we propose an easy algorithm to extrapolate the thickness of the diamond layer in a DOI substrate using colorimetric analysis. The algorithm consists of two parts: the first part is used for calibrating brightness on a sample with known thicknesses, and the second part is used to extrapolate the thickness of the diamond on the DOI under test using the previously-calibrated brightness.

With reference to Fig. 11, the first part of the algorithm begins with an image taken of a substrate whose thicknesses are at least approximately known. Ideally, this should be the same substrate on which the diamond layer is placed (bonded). This image is used to estimate the brightness of the system. The image is taken with a known illuminant, for example, the illuminant A for an incandescent lamp, as in standard microscopes, and without any optical filters. After white balance adjustment, the RGB values for this image are converted into XYZ coordinates using the relationships in the literature [92,94]. These transformations also account for the gamma correction associated with the monitors' sRGB or Adobe RGB color spaces. The XYZ coordinates are then converted into CIE LAB ($L^*a^*b^*$) coordinates using Eq. (8). Since the thickness of the reference system is known, the LAB coordinates can also be calculated theoretically. This is done by sweeping the brightness parameter (P) in Eq. (7), and, if needed, by varying the thickness around its known value. The source brightness, and at the same time the reference thickness, are then obtained from the condition that minimizes the total color difference (TCD) between the measured and calculated colors.

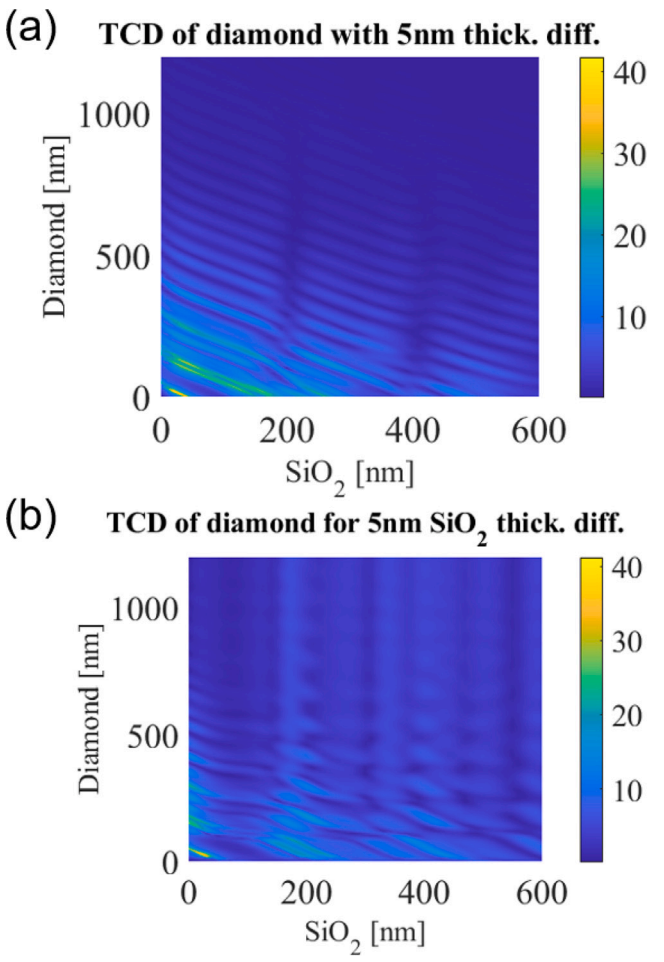


Fig. 10. Total Color Difference (TCD) for (a) diamond layers with 5 nm thickness difference, (b) diamond layers with same thickness laying on SiO_2 substrate with 5 nm layer thickness.

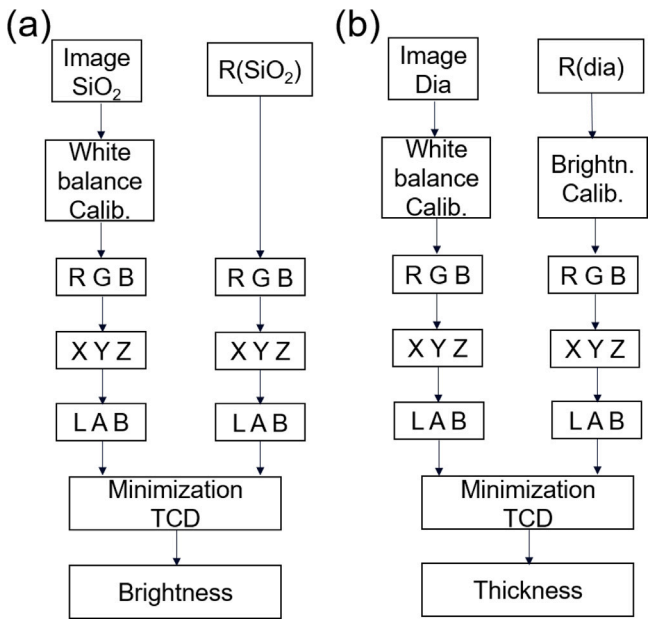


Fig. 11. Schematics of the colorimetric algorithm used for the extrapolation of the diamond thickness from an image: (a) first part of the algorithm in which the brightness of the image of a reference sample with known thickness is extrapolated by minimizing the TCD between the colors of the image and the calculated ones for the same system; (b) second part of the algorithm where the thicknesses of diamond in selected points of an image are extrapolated by minimizing the TCD of their color image and the calculated ones with the brightness calculated in (a).

In the second part of the algorithm, an image of the DOI sample under test is acquired under the same optical conditions used in the first part. The white balance is adjusted in the same way, and the RGB values are extracted from the points of interest. These values are converted into XYZ coordinates, calibrated using the brightness parameter (P) obtained in the first part of the algorithm, and then transformed into CIE LAB coordinates ($L^*a^*b^*$). Next, the system's reflectivities are calculated over a range of diamond thicknesses. The calculated reflectivity spectra are converted into XYZ coordinates and then transformed into LAB coordinates. The thickness of the diamond, which minimizes the TCD between the calculated and experimentally extrapolated coordinates, is assumed to be the effective thickness of the diamond layer.

Fig. 12 shows a concrete example of thickness extrapolation for a DOI sample with nominal diamond/SiO_2 thicknesses of 300 nm/300 nm The reference sample, shown in Fig. 12a, is a SiO_2/Si substrate without diamond and with a known SiO_2 thickness of 300 nm. The DOI substrate with diamond is shown in Fig. 12b where the red dot indicates the point of interest. The images were taken with a camera (Olympus SC30), attached to an optical microscope (Olympus BX51) with a 5X objective (Olympus MPLFLN 5X) of numerical aperture 0.15 and 2.65 mm of field of view. The exposure time was kept the same for both images. Because of the large field of view and the low numerical aperture, the incident light can be approximated as straight, with negligible angular spread.

In the frame of Fig. 12, we show the color obtained by minimization of the TCD. In this case, we varied the brightness and, in a small range, the thickness. In this case, the minimal TCD is obtained for a brightness of 84% and a SiO_2 thickness of 295 nm, quite close to the nominal thickness of 300 nm. Performing the second part of the algorithm with this brightness and SiO_2 thickness, we can similarly find that the thickness of the diamond at the point of interest is 304 nm. By comparing the thickness extrapolated from our analysis with the corresponding thickness measured by the WLI, we can assess that our method estimates the correct thickness within a range of ±3nm. This is remarkable considering the simplicity of the method, which can provide a good initial estimate of the diamond thickness [95]. To give a visual comparison of the color difference between similar diamond thicknesses, we added three frames at the bottom of Fig. 12b. These frames show, from left to right, the calculated colors for diamonds of thicknesses 290 nm, 300 nm, and 310 nm on the same substrate. The color that most closely resembles the diamond color in the image corresponds to 300 nm, which is also the closest value to the extrapolated diamond thickness. The process can also be automated to produce a thickness map over a full region of interest [96].

It is worth noting that this is a simple model, and a perfect match between the image and the simulation cannot be fully expected. Several factors are not completely controllable. First, the calibration of the light source and the white balance may not be ideally described by the chosen illuminant [85,97]. The refractive indices of the investigated materials may also differ from the literature values. In addition, the color transformations applied by the digital microscope hardware and software may not be perfectly described by the chosen color space. Second, the finite numerical aperture of the objective lens means that the incident light is not perfectly perpendicular to the sample, as assumed in the simulations [98]. These incident angles usually follow a Gaussian distribution [93,97,99], with a maximum incident angle $\theta_{max} = \arcsin(NA)$ in air. The corresponding optical paths produce different phases and, therefore, modify the reflectivity of the material. However, this effect is expected to be low or reduced for thinner films [93], and for the low numerical aperture used in this work.

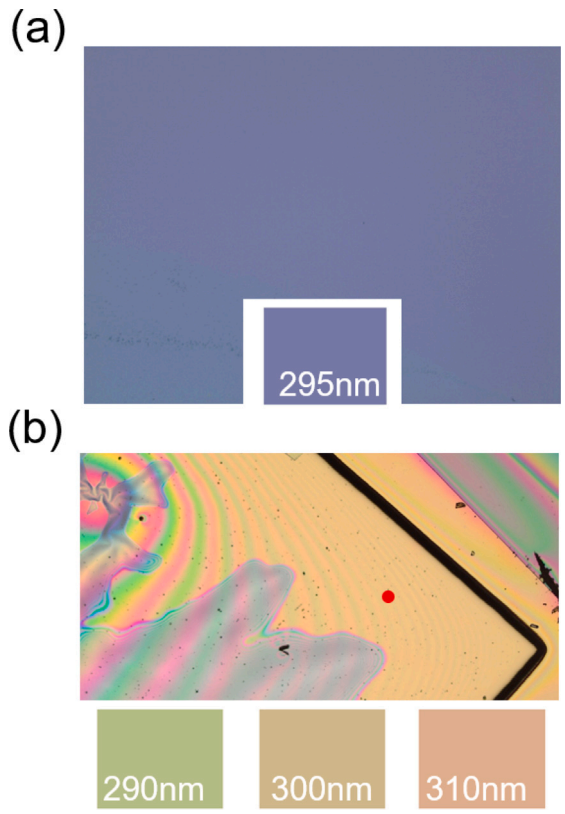


Fig. 12. Example of application of the method: (a) image of a sample with a known thickness (295 nm thick SiO_2 without diamond, 5X objective, halogen lamp), and, in the frame, calculated image minimizing the TCD with corresponding to the same thickness and a brightness of 84%, (b) image of a sample of which we want to extrapolate the thickness on diamond (located at the red dot) taken with the same condition and in the, frames, simulated colors for SiO_2 / Dia=295 nm/290 nm, SiO_2 / Dia=295 nm/300 nm, the closes in color among the three, and, SiO_2 / Dia=295 nm/310 nm.

8. Summary and conclusion

In this work, we developed a practical route for producing photonic-grade DOI substrates from directly bonded single-crystal diamond on SiO_2/Si. The main challenge was not only to remove several micrometers of diamond, but to do so without breaking the bonded interface or damaging the surface needed for low-loss nanophotonics. By comparing different plasma conditions and carrier configurations, we found that high-power etching can trigger debonding primarily through thermo-mechanical stress, whereas long oxygen-rich etches can lead to severe micromasking and nanopillar formation. These limitations were overcome by combining a quartz-assisted carrier/mask configuration with a cyclic ICP-RIE process consisting of Ar/Cl_2 cleaning/smoothing and Ar/O_2 diamond removal. Using this process, a 10 μm directly bonded diamond plate was thinned to an approximately 300 nm DOI film over a 0.5×0.5 mm^2 region, while maintaining an intact buried interface and sub-nanometer surface roughness.

The fabricated DOI film was further used to demonstrate free-standing frame-supported diamond photonic chiplets, showing that the substrate is compatible with standard lithography, dry etching, oxide release, and pick-and-place handling. In parallel, we developed a colorimetric thickness-evaluation method based on thin-film interference in the diamond/SiO_2/Si stack, enabling rapid thickness estimation from standard optical microscope images with about 5 nm resolution and good agreement with WLI measurements. Together, the optimized thinning process, chiplet demonstration, and simple optical metrology form a compact manufacturing platform for scalable diamond nanophotonics. This approach provides a direct path from bonded diamond plates to device-ready DOI substrates and can support scalable integration of diamond quantum photonic circuits, heterogeneous chiplets, and broader diamond-based photonic and electronic systems.

CRediT authorship contribution statement

Tianyin Chen: Writing – review & editing, Writing – original draft, Visualization, Validation, Resources, Methodology, Investigation, Formal analysis, Conceptualization. **Alessio Miranda:** Writing – review & editing, Writing – original draft, Visualization, Validation, Formal analysis, Data curation. **Leyla Rami:** Writing – review & editing, Writing – original draft, Visualization, Validation, Methodology, Investigation, Formal analysis, Data curation. **Ryoichi Ishihara:** Writing – review & editing, Supervision, Resources, Project administration, Funding acquisition, Conceptualization. **Salahuddin Nur:** Writing – review & editing, Writing – original draft, Visualization, Supervision, Resources, Project administration, Methodology, Investigation, Funding acquisition, Data curation, Conceptualization.

Declaration of competing interest

The authors declare the following financial interests/personal relationships which may be considered as potential competing interests: Salahuddin Nur reports financial support was provided by Fujitsu Ltd. Salahuddin Nur has patent Bonded diamond structures licensed to NL2035350B1. Ryoichi Ishihara has patent Bonded diamond structures licensed to NL2035350B1. If there are other authors, they declare that they have no known competing financial interests or personal relationships that could have appeared to influence the work reported in this paper.

Acknowledgments

We gratefully acknowledge support from the joint research program “Modular quantum computers” by Fujitsu Limited and Delft University of Technology, co-funded by the Netherlands Enterprise Agency under project number PPS2007.

Data availability

Data will be made available on request.

References

[1] C.M. Knaut, A. Suleymanzade, Y.-C. Wei, D.R. Assumpcao, P.-J. Stas, Y.Q. Huan, B. Machielse, E.N. Knall, M. Sutula, G. Baranes, N. Sinclair, C. De-Eknamkul, D.S. Levonian, M.K. Bhaskar, H. Park, M. Lončar, M.D. Lukin, Entanglement of nanophotonic quantum memory nodes in a telecom network, Nature 629 (8012) (2024) 573–578, http://dx.doi.org/10.1038/s41586-024-07252-z, URL https://www.nature.com/articles/s41586-024-07252-z.

[2] M. Xu, D. Wang, K. Fu, D.H. Mudiyanselage, H. Fu, Y. Zhao, A review of ultrawide bandgap materials: properties, synthesis and devices, Oxf. Open Mater. Sci. 2 (1) (2022) itac004, http://dx.doi.org/10.1093/oxfmat/itac004.

[3] I. Aharonovich, A.D. Greentree, S. Prawer, Diamond photonics, Nat. Photonics 5 (7) (2011) 397–405, http://dx.doi.org/10.1038/nphoton.2011.54, 10.1038/nphoton.2011.54.

[4] S. Prawer, I. Aharonovich, Quantum Information Processing with Diamond: Principles and Applications, first ed., Woodhead Publishing, Limited, 2018.

[5] M. Atatüre, D. Englund, N. Vamivakas, S.-Y. Lee, J. Wrachtrup, Material platforms for spin-based photonic quantum technologies, Nat. Rev. Mater. 491 (2018) 421, http://dx.doi.org/10.1038/s41578-018-0008-9.

[6] M. Ruf, N.H. Wan, H. Choi, D. Englund, R. Hanson, Quantum networks based on color centers in diamond, J. Appl. Phys. 130 (7) (2021) 070901, http://dx.doi.org/10.1063/5.0056534.

[7] G. Perez, A. Maréchal, G. Chicot, P. Lefranc, P.-O. Jeannin, D. Eon, N. Rouger, Diamond semiconductor performances in power electronics applications, Diam. Relat. Mater. 110 (2020) 108154, http://dx.doi.org/10.1016/j.diamond.2020.108154, URL https://www.sciencedirect.com/science/article/pii/S092596352030707X.

[8] N. Donato, N. Rouger, J. Pernot, G. Longobardi, F. Udrea, Diamond power devices: state of the art, modelling, figures of merit and future perspective, J. Phys. D: Appl. Phys. 53 (9) (2020) 093001, http://dx.doi.org/10.1088/1361-6463/ab4eab.

[9] M.M. Hasan, C. Wang, N. Pala, M. Shur, Diamond for high-power, high-frequency, and terahertz plasma wave electronics, Nanomaterials 14 (5) (2024) http://dx.doi.org/10.3390/nano14050460, URL https://www.mdpi.com/2079-4991/14/5/460.

[10] J. Liang, N. Shigekawa, Direct bonding of diamond and dissimilar materials for fabricating high performace power devices, in: S. Mandal, N. Yang (Eds.), Novel Aspects of Diamond II Science and Technology, in: Topics in Applied Physics, 2024, pp. 237–268, http://dx.doi.org/10.1007/978-3-031-47556-6_9.

[11] M. Angelone, C. Verona, Properties of diamond-based neutron detectors operated in harsh environments, J. Nucl. Eng. 2 (4) (2021) 422–470, http://dx.doi.org/10.3390/jne2040032, URL https://www.mdpi.com/2673-4362/2/4/32.

[12] V.K. Khanna, Diamond electronics for ultra-hot environments, in: Extreme-Temperature and Harsh-Environment Electronics (Second Edition), in: 2053-2563, IOP Publishing, 2023, pp. 10–1 to 10–33, http://dx.doi.org/10.1088/978-0-7503-5072-3ch10.

[13] H. Umezawa, Diamond semiconductor devices for harsh environmental applications, in: 2022 6th IEEE Electron Devices Technology & Manufacturing Conference, EDTM, 2022, pp. 297–299, http://dx.doi.org/10.1109/EDTM53872.2022.9798392.

[14] P. Latawiec, V. Venkataraman, M.J. Burek, B.J.M. Hausmann, I. Bulu, M. Lončar, On-chip diamond Raman laser, Optica 2 (11) (2015) 924–928, http://dx.doi.org/10.1364/optica.2.000924, arXiv:1509.00373.

[15] B.J.M. Hausmann, I. Bulu, V. Venkataraman, P. Deotare, M. Lončar, Diamond nonlinear photonics, Nat. Photonics 8 (5) (2014) 369–374, http://dx.doi.org/10.1038/nphoton.2014.72.

[16] R. Katsumi, K. Takada, F. Jelezko, T. Yatsui, Recent progress in hybrid diamond photonics for quantum information processing and sensing, Commun. Eng. 4 (1) (2025) 85, http://dx.doi.org/10.1038/s44172-025-00398-2, Publisher: Nature Publishing Group. URL https://www.nature.com/articles/s44172-025-00398-2.

[17] C. Bradac, W. Gao, J. Forneris, M.E. Trusheim, I. Aharonovich, Quantum nanophotonics with group IV defects in diamond, Nat. Commun. 10 (1) (2019) 5625, http://dx.doi.org/10.1038/s41467-019-13332-w.

[18] E. Janitz, M.K. Bhaskar, L. Childress, Cavity quantum electrodynamics with color centers in diamond, Optica 7 (10) (2020) 1232–1252, http://dx.doi.org/10.1364/OPTICA.398628, Publisher: Optica Publishing Group. URL https://opg.optica.org/optica/abstract.cfm?uri=optica-7-10-1232.

[19] S. Pezzagna, J. Meijer, Quantum computer based on color centers in diamond, Appl. Phys. Rev. 8 (1) (2021) 011308, http://dx.doi.org/10.1063/5.0007444.

[20] N. Mizuochi, T. Makino, H. Kato, D. Takeuchi, M. Ogura, H. Okushi, M. Nothaft, P. Neumann, A. Gali, F. Jelezko, J. Wrachtrup, S. Yamasaki, Electrically driven single-photon source at room temperature in diamond, Nat. Photonics 6 (5) (2012) 299–303, http://dx.doi.org/10.1038/nphoton.2012.75.

[21] C.G. Torun, M. Gokce, T.K. Bracht, M.I. Monsalve, S. Benbouabdellah, O.O. Nacitarhan, M.E. Stucki, D.B. Alvaro, M.L. Markham, T. Pregnolato, J.H.D. Munns, G. Pieplow, D.E. Reiter, T. Schröder, SUPER and femtosecond spin-conserving coherent excitation of a tin-vacancy color center in diamond, Nat. Commun. 17 (1) (2026) 2154, http://dx.doi.org/10.1038/s41467-026-69911-1, URL https://www.nature.com/articles/s41467-026-69911-1.

[22] R. Schirhagl, K. Chang, M. Loretz, C.L. Degen, Nitrogen-vacancy centers in diamond: Nanoscale sensors for physics and biology, Dx.Doi.Org 65 (1) (2014) 83–105, http://dx.doi.org/10.1146/annurev-physchem-040513-103659.

[23] E.V. Levine, M.J. Turner, P. Kehayias, C.A. Hart, N. Langellier, R. Trubko, D.R. Glenn, R.R. Fu, R.L. Walsworth, Principles and techniques of the quantum diamond microscope, Nanophotonics 8 (11) (2019) 1945–1973, http://dx.doi.org/10.1515/nanoph-2019-0209.

[24] Y. Wang, W. Zhang, H. Chai, Z. Zhang, S. Lin, X. Qin, J. Du, Fully integrated quantum magnetometer based on nitrogen-vacancy centers, Phys. Rev. Appl. 23 (3) (2025) 034008, http://dx.doi.org/10.1103/physrevapplied.23.034008.

[25] I. Varveris, G.D. Aliberti, F.J. Barzilaij, Z. Jin, S.A.v. Rijs, Q. Dong, D. Brinks, S. Nur, R. Ishihara, Toward a CMOS-integrated quantum diamond biosensor based on NV centers, 2026, http://dx.doi.org/10.48550/arxiv.2602.20437, arXiv:2602.20437 URL https://arxiv.org/abs/2602.20437.

[26] G.D. Fuchs, G. Burkard, P.V. Klimov, D.D. Awschalom, A quantum memory intrinsic to single nitrogen–vacancy centres in diamond, Nat. Phys. 7 (10) (2011) 789–793, http://dx.doi.org/10.1038/nphys2026.

[27] P.C. Maurer, G. Kucsko, C. Latta, L. Jiang, N.Y. Yao, S.D. Bennett, F. Pastawski, D. Hunger, N. Chisholm, M. Markham, D.J. Twitchen, J.I. Cirac, M.D. Lukin, Room-temperature quantum bit memory exceeding one second, Science 336 (6086) (2012) 1283–1286, http://dx.doi.org/10.1126/science.1220513, URL http://science.sciencemag.org/content/336/6086/1283.

[28] C.E. Bradley, S.W.d. Bone, P.F.W. Möller, S. Baier, M.J. Degen, S.J.H. Loenen, H.P. Bartling, M. Markham, D.J. Twitchen, R. Hanson, D. Elkouss, T.H. Taminiau, Robust quantum-network memory based on spin qubits in isotopically engineered diamond, Npj Quantum Inf. 8 (1) (2022) 122, http://dx.doi.org/10.1038/s41534-022-00637-w.

[29] M. Pompili, S.L.N. Hermans, S. Baier, H.K.C. Beukers, P.C. Humphreys, R.N. Schouten, R.F.L. Vermeulen, M.J. Tiggelman, L.d.S. Martins, B. Dirkse, S. Wehner, R. Hanson, Realization of a multinode quantum network of remote solid-state qubits, Science 372 (6539) (2021) 259–264, http://dx.doi.org/10.1126/science.abg1919, arXiv:2102.04471.

[30] P.-J. Stas, Y.-C. Wei, M. Sirotin, Y.Q. Huan, U. Yazlar, F.A. Arias, E. Knyazev, G. Baranes, B. Machielse, S. Grandi, D. Riedel, J. Borregaard, H. Park, M. Lončar, A. Suleymanzade, M.D. Lukin, Entanglement-assisted non-local optical interferometry in a quantum network, Nature 651 (8105) (2026) 326–332, http://dx.doi.org/10.1038/s41586-026-10171-w, arXiv:2509.09464.

[31] P.K. Shandilya, S. Flgan, N.C. Carvalho, E. Zohari, V.K. Kavatamane, J.E. Losby, P.E. Barclay, Diamond integrated quantum nanophotonics: Spins, photons and phonons, IEEE/OSA J. Light. Technol. 40 (23) (2022) 7538–7571, http://dx.doi.org/10.1109/jlt.2022.3210466, arXiv:2207.08844.

[32] D.D. Awschalom, R. Hanson, J. Wrachtrup, B.B. Zhou, Quantum technologies with optically interfaced solid-state spins, Nat. Photonics 12 (9) (2018) 516–527, http://dx.doi.org/10.1038/s41566-018-0232-2, URL https://www.nature.com/articles/s41566-018-0232-2.

[33] R. Ishihara, J. Hermias, S. Yu, K.Y. Yu, Y. Li, S. Nur, T. Iwai, T. Miyatake, K. Kawaguchi, Y. Doi, S. Sato, 3D Integration Technology for Quantum Computer based on Diamond Spin Qubits, in: 2021 IEEE International Electron Devices Meeting (IEDM), IEEE, San Francisco, CA, USA, 2021, pp. 14.5.1–14.5.4, http://dx.doi.org/10.1109/IEDM19574.2021.9720552.

[34] N.H. Wan, T.-J. Lu, K.C. Chen, M.P. Walsh, M.E. Trusheim, L.D. Santis, E.A. Bersin, I.B. Harris, S.L. Mouradian, I.R. Christen, E.S. Bielejec, D. Englund, Large-scale integration of artificial atoms in hybrid photonic circuits, Nature 583 (2020) 226–231, http://dx.doi.org/10.1038/s41586-020-2441-3, URL https://www.nature.com/articles/s41586-020-2441-3 arXiv:1911.05265.

[35] S.W. Ding, C. Jin, K. Kuruma, X. Guo, M. Haas, B. Korzh, A. Beyer, M.D. Shaw, N. Sinclair, D.D. Awschalom, F.J. Heremans, N. Delegan, A.A. High, M. Loncar, Purcell-enhanced emissions from diamond color centers in slow light photonic crystal waveguides, Nano Lett. 25 (32) (2025) 12125–12131, http://dx.doi.org/10.1021/acs.nanolett.5c01079.

[36] J. Fischer, Y. Herrmann, C.F.J. Wolfs, S. Scheijen, M. Ruf, R. Hanson, Spin-photon correlations from a purcell-enhanced diamond nitrogen-vacancy center coupled to an open microcavity, Nat. Commun. 16 (1) (2025) 11680, http://dx.doi.org/10.1038/s41467-025-66722-8, arXiv:2506.20722.

[37] S.W. Ding, M. Haas, X. Guo, K. Kuruma, C. Jin, Z. Li, D.D. Awschalom, N. Delegan, F.J. Heremans, A.A. High, M. Loncar, High-q cavity interface for color centers in thin film diamond, Nat. Commun. 15 (1) (2024) 6358, http://dx.doi.org/10.1038/s41467-024-50667-5, Publisher: Nature Publishing Group. URL https://www.nature.com/articles/s41467-024-50667-5.

[38] A.E. Rugar, S. Aghaeimeibodi, D. Riedel, C. Dory, H. Lu, P.J. McQuade, Z.-X. Shen, N.A. Melosh, J. Vučković, Quantum Photonic Interface for Tin-Vacancy Centers in Diamond, Phys. Rev. X 11 (3) (2021) 031021, http://dx.doi.org/10.1103/PhysRevX.11.031021, Publisher: American Physical Society. URL https://link.aps.org/doi/10.1103/PhysRevX.11.031021.

[39] H. Lee, H.C. Kleidermacher, A.J. Stein, H. Oh, L.B.H. Wyatt, C.K. Kim, L. Basso, A.M. Mounce, Y. Wang, S.S. Su, M. Titze, A.C.B. Jayich, J. Vučković, Quantum nanophotonic interface for tin-vacancy centers in thin-film diamond, Phys. Rev. Appl. 25 (4) (2026) 044074, http://dx.doi.org/10.1103/vwt7-b64x.

[40] D. Riedel, T. Graziosi, Z. Wang, C. De-Eknamkul, A. Abulnaga, J. Dietz, A. Mucchietto, M. Haas, M. Sutula, P. Barral, M. Pompili, M. Raha, C. Robens, J. Ha, D. Sukachev, D. Levonian, M. Bhaskar, M. Markham, B. Machielse, Scalable photonic quantum interconnect platform, Phys. Rev. X 16 (1) (2026) 011063, http://dx.doi.org/10.1103/nfrg-zsts.

[41] D. Rani, O.R. Opaluch, E. Neu, Recent advances in single crystal diamond device fabrication for photonics, sensing and nanomechanics, Micromachines 12 (1) (2020) 36, http://dx.doi.org/10.3390/mi12010036.

[42] P. Hill, E. Gu, M.D. Dawson, M.J. Strain, Thin film diamond membranes bonded on-demand with SOI ring resonators, Diam. Relat. Mater. 88 (2018) 215–221, http://dx.doi.org/10.1016/j.diamond.2018.07.020.

[43] A.H. Piracha, P. Rath, K. Ganesan, S. Kühn, W.H.P. Pernice, S. Prawer, Scalable Fabrication of Integrated Nanophotonic Circuits on Arrays of Thin Single Crystal Diamond Membrane Windows, Nano Lett. 16 (5) (2016) 3341–3347, http://dx.doi.org/10.1021/acs.nanolett.6b00974, Publisher: American Chemical Society.

[44] V. Uwihoreye, Y. Hu, G. Cao, X. Zhang, F.E. Oropeza, K.H.L. Zhang, Recent progress on heteroepitaxial growth of single crystal diamond films, Electron 2 (4) (2024) http://dx.doi.org/10.1002/elt2.70.

[45] H. Bensalah, I. Stenger, G. Sakr, J. Barjon, R. Bachelet, A. Tallaire, J. Achard, N. Vaissiere, K. Lee, S. Saada, J. Arnault, Mosaicity, dislocations and strain in heteroepitaxial diamond grown on iridium, Diam. Relat. Mater. 66 (2016) 188–195, http://dx.doi.org/10.1016/j.diamond.2016.04.006.

[46] S. Mandal, Nucleation of diamond films on heterogeneous substrates: a review, RSC Adv. 11 (17) (2021) 10159–10182, http://dx.doi.org/10.1039/d1ra00397f.

[47] T. Chen, J. Hermias, S. Nur, R. Ishihara, Hydrophilic direct bonding of (100) diamond and deposited SiO2 substrates, Appl. Phys. Lett. 126 (23) (2025) 231901, http://dx.doi.org/10.1063/5.0263008.

[48] M.J. Burek, Y. Chu, M.S.Z. Liddy, P. Patel, J. Rochman, S. Meesala, W. Hong, Q. Quan, M.D. Lukin, M. Lončar, High quality-factor optical nanocavities in bulk single-crystal diamond, Nat. Commun. 5 (2014) 5718, http://dx.doi.org/10.1038/ncomms6718, URL http://www.nature.com/ncomms/2014/141216/ncomms6718/full/ncomms6718.html.

[49] J.C. Lee, A.P. Magyar, D.O. Bracher, I. Aharonovich, E.L. Hu, Fabrication of thin diamond membranes for photonic applications, Diam. Relat. Mater. 33 (2013) 45–48, http://dx.doi.org/10.1016/j.diamond.2012.12.008.

[50] X. Guo, N. Delegan, J.C. Karsch, Z. Li, T. Liu, R. Shreiner, A. Butcher, D.D. Awschalom, F.J. Heremans, A.A. High, Tunable and Transferable Diamond Membranes for Integrated Quantum Technologies, Nano Lett. 21 (24) (2021) 10392–10399, http://dx.doi.org/10.1021/acs.nanolett.1c03703, Publisher: American Chemical Society.

[51] X. Guo, M. Xie, A. Addhya, A. Linder, U. Zvi, S. Wang, X. Yu, T.D. Deshmukh, Y. Liu, I.N. Hammock, Z. Li, C.T. DeVault, A. Butcher, A.P. Esser-Kahn, D.D. Awschalom, N. Delegan, P.C. Maurer, F.J. Heremans, A.A. High, Direct-bonded diamond membranes for heterogeneous quantum and electronic technologies, Nat. Commun. 15 (1) (2024) 8788, http://dx.doi.org/10.1038/s41467-024-53150-3.

[52] B. Khanaliloo, M. Mitchell, A.C. Hryciw, P.E. Barclay, High-q/v monolithic diamond microdisks fabricated with quasi-isotropic etching, Nano Lett. 15 (8) (2015) 5131–5136, http://dx.doi.org/10.1021/acs.nanolett.5b01346, PMID: 26134379.

[53] S. Mi, M. Kiss, T. Graziosi, N. Quack, Integrated photonic devices in single crystal diamond, J. Phys.: Photonics 2 (4) (2020) 042001, http://dx.doi.org/10.1088/2515-7647/aba171, Publisher: IOP Publishing.

[54] A. Miranda, R. Ishihara, S. Nur, Cross waveguide design for color-centers in diamond for photonic quantum computing, 2026, http://dx.doi.org/10.48550/arxiv.2604.19594, arXiv. URL https://arxiv.org/abs/2604.19594 arXiv:2604.19594.

[55] A. Corazza, S. Ruffieux, Y. Zhu, C.A.J. Concha, Y. Fontana, C. Galland, R.J. Warburton, P. Maletinsky, Homogeneous free-standing nanostructures from bulk diamond over millimeter scales for quantum technologies, Nano Lett. 25 (40) (2025) 14526–14533, http://dx.doi.org/10.1021/acs.nanolett.5c03083.

[56] M. Bruel, Silicon on insulator material technology, Electron. Lett. 31 (14) (1995) 1201–1202, http://dx.doi.org/10.1049/el:19950805.

[57] W. Bogaerts, D. Taillaert, B. Luyssaert, P. Dumon, J.V. Campenhout, P. Bienstman, D.V. Thourhout, R. Baets, V. Wiaux, S. Beckx, Basic structures for photonic integrated circuits in silicon-on-insulator, Opt. Express 12 (8) (2004) 1583, http://dx.doi.org/10.1364/opex.12.001583.

[58] A. Plößl, G. Kräuter, Silicon-on-insulator: materials aspects and applications, Solid-State Electron. 44 (5) (2000) 775–782, http://dx.doi.org/10.1016/s0038-1101(99)00273-7.

[59] Y.A. Vlasov, S.J. McNab, Losses in single-mode silicon-on-insulator strip waveguides and bends, Opt. Express 12 (8) (2004) 1622, http://dx.doi.org/10.1364/opex.12.001622.

[60] K. Ashida, M. Okano, T. Yasuda, M. Ohtsuka, M. Seki, N. Yokoyama, K. Koshino, K. Yamada, Y. Takahashi, Photonic crystal nanocavities with an average q factor of 1.9 million fabricated on a 300-mm-wide SOI wafer using a CMOS-compatible process, J. Lightwave Technol. 36 (20) (2018) 4774–4782, http://dx.doi.org/10.1109/jlt.2018.2861894.

[61] S. Nur, H.-J. Lim, J. Elzerman, J.J.L. Morton, Silicon photonic crystal cavities at near band-edge wavelengths, Appl. Phys. Lett. 114 (9) (2019) 091101, http://dx.doi.org/10.1063/1.5067358.

[62] G.T. Reed, G. Mashanovich, F.Y. Gardes, D.J. Thomson, Silicon optical modulators, Nat. Photonics 4 (8) (2010) 518–526, http://dx.doi.org/10.1038/nphoton.2010.179.

[63] B. Khanaliloo, H. Jayakumar, A.C. Hryciw, D.P. Lake, H. Kaviani, P.E. Barclay, Single-crystal diamond nanobeam waveguide optomechanics, Phys. Rev. X 5 (4) (2015) 041051, http://dx.doi.org/10.1103/physrevx.5.041051.

[64] A. Sipahigil, R.E. Evans, D.D. Sukachev, M.J. Burek, J. Borregaard, M.K. Bhaskar, C.T. Nguyen, J.L. Pacheco, H.A. Atikian, C. Meuwly, R.M. Camacho, F. Jelezko, E. Bielejec, H. Park, M. Lončar, M.D. Lukin, An integrated diamond nanophotonics platform for quantum-optical networks, Science 354 (6314) (2016) 847–850, http://dx.doi.org/10.1126/science.aah6875, Publisher: American Association for the Advancement of Science. URL https://www.science.org/doi/10.1126/science.aah6875.

[65] M. Pasini, N. Codreanu, T. Turan, A.R. Moral, C.F. Primavera, L.D. Santis, H.K.C. Beukers, J.M. Brevoord, C. Waas, J. Borregaard, R. Hanson, Nonlinear quantum photonics with a tin-vacancy center coupled to a one-dimensional diamond waveguide, Phys. Rev. Lett. 133 (2) (2024) 023603, http://dx.doi.org/10.1103/physrevlett.133.023603, arXiv:2311.12927.

[66] N. Jiang, S. Noguchi, K. Nishimura, T. Inaoka, Y. Shintani, A. Hiraki, Growth and characterization of diamond films on SiO2/si substrates, Japan. J. Appl. Phys. 41 (11R) (2002) 6493, http://dx.doi.org/10.1143/jjap.41.6493.

[67] W. Wang, B. Liu, L. Zhang, J. Han, K. Liu, B. Dai, J. Zhu, Heteroepitaxy of diamond semiconductor on iridium: a review, Funct. Diam. 2 (1) (2022) 215–235, http://dx.doi.org/10.1080/26941112.2022.2162348.

[68] J. Chrétien, P. Gilles, F. Milesi, F. Berger, N. Bernier, N. Gauthier, G. Lapertot, C. Lecouvey, D. Mariolle, L. Colonel, P. Acosta Alba, F. Mazen, J. Widiez, I. Huyet, L. Le Van-Jodin, Transfer of diamond thin films using Smart Cut™ technology, Diam. Relat. Mater. 155 (2025) 112295, http://dx.doi.org/10.1016/j.diamond.2025.112295, URL https://www.sciencedirect.com/science/article/pii/S0925963525003528.

[69] M. Ruf, M. IJspeert, S. van Dam, N. de Jong, H. van den Berg, G. Evers, R. Hanson, Optically Coherent Nitrogen-Vacancy Centers in Micrometer-Thin Etched Diamond Membranes, Nano Lett. 19 (6) (2019) 3987–3992, http://dx.doi.org/10.1021/acs.nanolett.9b01316, Publisher: American Chemical Society.

[70] M.-L. Hicks, A.C. Pakpour-Tabrizi, R.B. Jackman, Diamond Etching Beyond 10 μm with Near-Zero Micromasking, Sci. Rep. 9 (1) (2019) 15619, http://dx.doi.org/10.1038/s41598-019-51970-8, Publisher: Nature Publishing Group. URL https://www.nature.com/articles/s41598-019-51970-8.

[71] A. Toros, M. Kiss, T. Graziosi, S. Mi, R. Berrazouane, M. Naamoun, J. Vukajlovic Plestina, P. Gallo, N. Quack, Reactive ion etching of single crystal diamond by inductively coupled plasma: State of the art and catalog of recipes, Diam. Relat. Mater. 108 (2020) 107839, http://dx.doi.org/10.1016/j.diamond.2020.107839, URL https://www.sciencedirect.com/science/article/pii/S0925963520300406.

[72] J. Heupel, M. Pallmann, J. Körber, R. Merz, M. Kopnarski, R. Stöhr, J.P. Reithmaier, D. Hunger, C. Popov, Fabrication and Characterization of Single-Crystal Diamond Membranes for Quantum Photonics with Tunable Microcavities, Micromachines 11 (12) (2020) 1080, http://dx.doi.org/10.3390/mi11121080, Publisher: Multidisciplinary Digital Publishing Institute. URL https://www.mdpi.com/2072-666X/11/12/1080.

[73] M.J. Burek, N.P. de Leon, B.J. Shields, B.J.M. Hausmann, Y. Chu, Q. Quan, A.S. Zibrov, H. Park, M.D. Lukin, M. Lončar, Free-standing mechanical and photonic nanostructures in single-crystal diamond, Nano Lett. 12 (12) (2012) 6084–6089, http://dx.doi.org/10.1021/nl302541e, PMID: 23163557.

[74] M.-L. Hicks, A.C. Pakpour-Tabrizi, V. Zuerbig, L. Kirste, C. Nebel, R.B. Jackman, Optimizing reactive ion etching to remove sub-surface polishing damage on diamond, J. Appl. Phys. 125 (24) (2019) 244502, http://dx.doi.org/10.1063/1.5094751.

[75] M.-L. Hicks, A.C. Pakpour-Tabrizi, R.B. Jackman, Polishing, preparation and patterning of diamond for device applications, Diam. Relat. Mater. 97 (2019) 107424, http://dx.doi.org/10.1016/j.diamond.2019.05.010, URL https://www.sciencedirect.com/science/article/pii/S0925963519302201.

[76] D.S. Hwang, T. Saito, N. Fujimori, New etching process for device fabrication using diamond, Proceedings of the 9th International Conference on New Diamond Science and Technology (ICNDST-9), Diam. Relat. Mater. 13 (11) (2004) 2207–2210, http://dx.doi.org/10.1016/j.diamond.2004.07.020, URL https://www.sciencedirect.com/science/article/pii/S0925963504002572.

[77] J. Enlund, J. Isberg, M. Karlsson, F. Nikolajeff, J. Olsson, D.J. Twitchen, Anisotropic dry etching of boron doped single crystal CVD diamond, Carbon 43 (9) (2005) 1839–1842, http://dx.doi.org/10.1016/j.carbon.2005.02.022, URL https://www.sciencedirect.com/science/article/pii/S0008622305001284.

[78] B.J.M. Hausmann, M. Khan, Y. Zhang, T.M. Babinec, K. Martinick, M. McCutcheon, P.R. Hemmer, M. Lončar, Fabrication of diamond nanowires for quantum information processing applications, Proceedings of Diamond 2009, The 20th European Conference on Diamond, Diamond-Like Materials, Carbon Nanotubes and Nitrides, Part 1, Diam. Relat. Mater. 19 (5) (2010) 621–629, http://dx.doi.org/10.1016/j.diamond.2010.01.011, URL https://www.sciencedirect.com/science/article/pii/S0925963510000312.

[79] C.L. Lee, E. Gu, M.D. Dawson, I. Friel, G.A. Scarsbrook, Etching and micro-optics fabrication in diamond using chlorine-based inductively-coupled plasma, Proceedings of Diamond 2007, the 18th European Conference on Diamond, Diamond-Like Materials, Carbon Nanotubes, Nitrides and Silicon Carbide, Diam. Relat. Mater. 17 (7) (2008) 1292–1296, http://dx.doi.org/10.1016/j.diamond.2008.01.011, URL https://www.sciencedirect.com/science/article/pii/S0925963508000174.

[80] P.F. Egan, Expansivity of fused quartz glass measured within 6× 10-10k-1, Int. J. Thermophys. 45 (9) (2024) 131, http://dx.doi.org/10.1007/s10765-024-03422-3.

[81] A. Kelly, Composite materials for thermal expansivity matching and high heat flux thermal management, Key Eng. Mater. 334–335 (2007) 1017–1020, http://dx.doi.org/10.4028/www.scientific.net/kem.334-335.1017.

[82] J. Haisma, B.A.C.M. Spierings, U.K.P. Biermann, A.A. Van Gorkum, Diversity and feasibility of direct bonding: A survey of a dedicated optical technology, Appl. Opt. 33 (7) (1994) 1154, http://dx.doi.org/10.1364/AO.33.001154.

[83] N. Codreanu, Diamond Nanophotonic Devices for Quantum Networks Experiments (Ph.D. thesis), Delft University of Technology, 2025, URL https://repository.tudelft.nl/record/uuid:e1c789d7-d71e-42b8-a9a8-23fafdaea22e.

[84] L. Rami, et al., Optimization of pick and place integration of diamond chiplets on SiN waveguides. (in preparation).

[85] M.R. Müller, A. Gumprich, E. Ecik, K.T. Kallis, F. Winkler, B. Kardynal, I. Petrov, U. Kunze, J. Knoch, Visibility of two-dimensional layered materials on various substrates, J. Appl. Phys. 118 (14) (2015-10-14) 145305, http://dx.doi.org/10.1063/1.4930574, URL https://pubs.aip.org/jap/article/118/14/145305/139434/Visibility-of-two-dimensional-layered-materials-on.

[86] P. Blake, E.W. Hill, A.H. Castro Neto, K.S. Novoselov, D. Jiang, R. Yang, T.J. Booth, A.K. Geim, Making graphene visible, Appl. Phys. Lett. 91 (6) (2007-08-06) 063124, http://dx.doi.org/10.1063/1.2768624, URL https://pubs.aip.org/apl/article/91/6/063124/1023191/Making-graphene-visible.

[87] A. Miranda, J. Halim, A. Lorke, M.W. Barsoum, Rendering $Ti_3C_2T_x$ (MXene) monolayers visible, Mater. Res. Lett. 5 (5) (2017-09-03) 322–328, http://dx.doi.org/10.1080/21663831.2017.1280707, URL https://www.tandfonline.com/doi/full/10.1080/21663831.2017.1280707.

[88] H.R. Phillip, E.A. Taft, Kramers-kronig analysis of reflectance data for diamond, Phys. Rev. 136 (5) (1964-11-30) A1445–A1448, http://dx.doi.org/10.1103/PhysRev.136.A1445, URL https://link.aps.org/doi/10.1103/PhysRev.136.A1445.

[89] C.M. Herzinger, B. Johs, W.A. McGahan, J.A. Woollam, W. Paulson, Ellipsometric determination of optical constants for silicon and thermally grown silicon dioxide via a multi-sample, multi-wavelength, multi-angle investigation, J. Appl. Phys. 83 (6) (1998-03-15) 3323–3336, http://dx.doi.org/10.1063/1.367101, URL https://pubs.aip.org/jap/article/83/6/3323/487646/Ellipsometric-determination-of-optical-constants.

[90] G. Ghosh, Dispersion-equation coefficients for the refractive index and birefringence of calcite and quartz crystals, Opt. Commun. 163 (1) (1999-05) 95–102, http://dx.doi.org/10.1016/S0030-4018(99)00091-7, URL https://linkinghub.elsevier.com/retrieve/pii/S0030401899000917.

[91] G.E. Jellison, M.F. Chisholm, S.M. Gorbatkin, Optical functions of chemical vapor deposited thin-film silicon determined by spectroscopic ellipsometry, Appl. Phys. Lett. 62 (25) (1993-06-21) 3348–3350, http://dx.doi.org/10.1063/1.109067, URL https://pubs.aip.org/apl/article/62/25/3348/526658/Optical-functions-of-chemical-vapor-deposited-thin.

[92] J. Schanda, Colorimetry: understanding the CIE system, John Wiley & sons, 2007, http://dx.doi.org/10.1002/9780470175637, URL https://onlinelibrary.wiley.com/doi/book/10.1002/9780470175637.

[93] L. Gao, W. Ren, F. Li, H.-M. Cheng, Total color difference for rapid and accurate identification of graphene, ACS Nano 2 (8) (2008-08-26) 1625–1633, http://dx.doi.org/10.1021/nn800307s, URL https://pubs.acs.org/doi/10.1021/nn800307s.

[94] http://www.brucelindbloom.com.

[95] A.R. Smith, Color gamut transform pairs, ACM SIGGRAPH Comput. Graph. 12 (3) (1978-08-23) 12–19, http://dx.doi.org/10.1145/965139.807361, URL https://dl.acm.org/doi/10.1145/965139.807361.

[96] C.M. Nolen, G. Denina, D. Teweldebrhan, B. Bhanu, A.A. Balandin, High-throughput large-area automated identification and quality control of graphene and few-layer graphene films, ACS Nano 5 (2) (2011-02-22) 914–922, http://dx.doi.org/10.1021/nn102107b, URL https://pubs.acs.org/doi/10.1021/nn102107b.

[97] W. Ouyang, X.-Z. Liu, Q. Li, Y. Zhang, J. Yang, Q.-s. Zheng, Optical methods for determining thicknesses of few-layer graphene flakes, Nanotechnology 24 (50) (2013-12-20) 505701, http://dx.doi.org/10.1088/0957-4484/24/50/505701, URL https://iopscience.iop.org/article/10.1088/0957-4484/24/50/505701.

[98] S. Roddaro, P. Pingue, V. Piazza, V. Pellegrini, F. Beltram, The optical visibility of graphene: Interference colors of ultrathin graphite on SiO_2, Nano Lett. 7 (9) (2007-09-01) 2707–2710, http://dx.doi.org/10.1021/nl071158l, URL https://pubs.acs.org/doi/10.1021/nl071158l.

[99] I. Jung, J.-S. Rhyee, J.Y. Son, R.S. Ruoff, K.-Y. Rhee, Colors of graphene and graphene-oxide multilayers on various substrates, Nanotechnology 23 (2) (2012-01-20) 025708, http://dx.doi.org/10.1088/0957-4484/23/2/025708, URL https://iopscience.iop.org/article/10.1088/0957-4484/23/2/025708.